Medical Instrumentation & Imaging Abstracts

Session – Medical Imaging 1
Room 3, Thursday 3 May, 09.00 – 10.30

Machine vision and texture analysis for the automated identification of tissue pattern in prostatic neoplasia

James Diamond[a]*, Neil H. Anderson[b], Peter H. Bartels[c], Rodolfo Montoroni[d] and Peter W. Hamilton[a]

[a] *Quantitative Biomarkers Group, Dept. Pathology, Cancer Research Centre, The Queen's University of Belfast, Grosvenor Road, Belfast, Northern Ireland*
[b] *Royal Hospital Trust, Belfast, N. Ireland, U.K.*
[c] *The Optical Sciences Center, University of Arizona, Tucson, Arizona, U.S.A.*
[d] *Institute of Pathological Anatomy and Histopathology, University of Ancona, Ancona, Italy.*

Introduction: Recent estimates have placed prostate cancer as the most commonly diagnosed malignancy, and the second leading cause of cancer death among men in the United States. The continuing challenge to the scientific and medical communities is to develop successful strategies for treatment and early identification of prostate cancer. Central to early identification are the concepts of quantitation and automation. The quantitative examination of prostate histology offers new clues in the diagnostic classification of prostatic lesions. In order to facilitate the collection of quantitative histometric data, automation is necessary. This is made possible through the development of machine vision systems for digital imagery. The aim of this study was to explore the use of image texture analysis for the automated identification of tissue abnormalities in low-power scans of prostate histology.

Methods: Ten whole mount sections taken from radical prostatectomies, which had been formalin fixed and paraffin wax-embedded were retrieved from file at The Institute of Pathological Anatomy and Histopathology, University of Ancona, Italy. Five micrometre sections were cut and stained routinely with haematoxylin and eosin. These were routinely assessed by a pathologist and graded as showing stroma (S), Benign Prostatic Hyperplasia (BPH) and carcinoma (C).

Image analysis was implemented using the Zeiss KS400 imaging system. This system provides the ability to sequence lower level image processing functions into a sequence termed a macro. In this way it is possible to implement a search rationale for processing an image. A macro was designed to integrate texture analysis, classification rules, which could generate digital maps of tissue pattern allowing the identification of areas of S, BPH and C. All texture features implemented in the KS400 system are after Haralick.

Results: Previous studies have shown that a sub-region size of 256 pixels is optimal. However, in this study it was deemed necessary to consider was any statistical reasoning valid in identifying this optimal

size. In assessing this, a range of sub-region sizes (100 - 250 pixels) was applied to the training images. The discriminatory ability of the system was considered for S/BPH, S/C and BPH/C. The results of these tests suggested that the discriminatory power of the system was maximised at around 200 pixels.

A training image set was collected providing exemplar patterns for S, BPH and C. An integrated software package was developed which subdivided the image into sub-regions of 200x200 pixels and subjected each to textural analysis. From this training set of data, discriminant functions based on a reduced set of features could be defined for the classification of S, BPH and C. The software was designed to integrate classification rules and generate digital maps of tissue pattern allowing the identification of areas of S, BPH and C.

A total of 10 histological scenes were interrogated by the machine vision system. The classification rules were used to generate digital maps of tissue pattern allowing the classification of sub-regions (n = 1871) of S, BPH and C. 70% of all test regions were correctly classified. An example of scene classification is shown in Fig. 1.
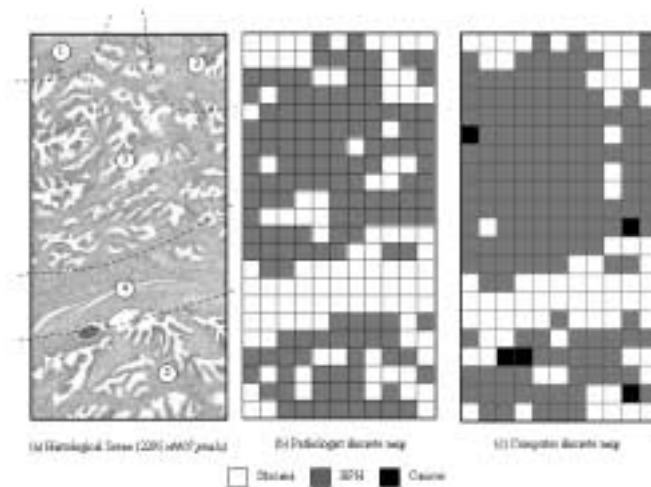

Fig. 1 – Automated scene segmentation

Discussion: This paper presents a methodology for inclusion in an automated system for the identification and classification of tissue pattern in prostatic neoplasia. It implements texture analysis algorithms in the low power scanning of large-scale histological scenes to achieve classification. The resulting regions from this classification could provide the basis for a more adaptive approach to quantifying the extent of glandular abnormality by only having to process those regions considered necessary. Here, approaches using more classical image processing techniques would be appropriate in quantifying glandular structures. This dual-level approach to processing takes its precedent from clinical practice whereby the pathologist will examine the slide at various magnifications. The practical application described in this paper offers a strong motivation for pursuing the scientific studies. Achieving the practical benefits of automated systems is achieved in combination with obtaining a deeper scientific understanding of many issues inherent in pathological diagnosis.

List-mode iterative reconstruction for SPECT

L Bouwens, M Koole, Y D'Asseler, S Vandenberghe, R Van de Walle and I Lemahieu
ELIS Department, MEDISIP, Ghent University, Sint-Pietersnieuwstraat 41 B-9000 Ghent, Belgium

Introduction: List-mode acquisition of single photon emission computed tomography (SPECT) projection data provides several advantages over that of frame mode acquisitions. Firstly, one can store the interaction location to a high degree of accuracy (2k by 2k for example) with greater efficiency than achievable with frame mode acquisition. Secondly, one does not need to bin the gantry angles into predefined frames, but can record the actual angle thereby removing the impact of angular blurring with continuous acquisition. Thirdly, one can record the actual energy of the interaction instead of attributing the event's energy to one of a limited number of pre-defined windows. When increasing the dimensionality in this way it is no longer possible to bin the data into a matrix. The array for binned data into a 2k x 2k matrix, for 360 detector angles and 10 energy bins would contain over 15 billion elements. Storing the acquired events with their parameters can result in a reduction in the required data space with a factor of over 2500. The result is a significant increase in the fidelity of recording the projection data, without a tremendous increase in storage space.

In this paper we propose a new projection operator having the ability to be changed easily according to the system specified. With this projector/backprojector pair we will proposes a new method for list-mode reconstruction in SPECT.

Method : Emission Radiance Distribution: Consider the object space surrounded by a convex enclosure (Figure 1). In this paper, we use a circular enclosure and will refer to it as the intermediate layer. The first step in our projector is to calculate the emission radiance distribution F for this layer. Properly normalized this distribution can be seen as the probability density surface for detecting a photon at a certain scanning point going in a specific direction.
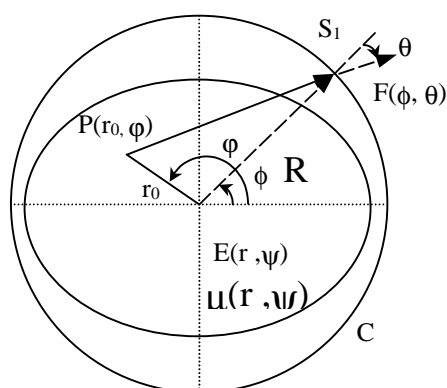

Fig.1.

Sampling Radiance with Collimated Detector: The collimator discussed in this paper is a parallel hole collimator. We place a collimator hole over the center of each of the detector bins. Seen from the collimator hole towards the intermediate layer, (i.e. the circle shown in Figure 2-3), we will see a fraction of the circle. The arc seen is restricted by the lines drawn from the outer most parts of the collimator holes, over the edges of collimator septa, to the circle. Next we obtain region $A(\phi,\theta)$ which is the portion of $F(\phi,\theta)$ from which photons can reach the detector location under investigation. When we integrate the emission radiance distribution $F(\phi,\theta)$ over the region $A(\phi,\theta)$, we get the contribution of the emitted photons from the total source distribution into the specific detector bin during projection. In the backprojection step, $A(\phi,\theta)$ defines the region into which the detector bin will contribute.

LMIRA: List-Mode Iterative Reconstruction Algorithm. The source estimate at each location l will be projected into the (ϕ,θ) space yielding F(ϕ,θ). This projection will be restricted by the list-mode specific acceptance region A(ϕ,θ) of the camera. This can be interpreted as the fraction of the isotropic photon emission from location l that can lead to this list-mode event.

The second part of the expression can be derived by sampling the emission radiance distribution F(ϕ,θ) using the region A(ϕ,θ), which will be the fraction of the total photon emission that can lead to this list-mode event. Therefore, the equation can be rewritten as follows:

$$f_l^{(t+1)} = \sum_{j=1}^{N} \frac{\iint\limits_{A_j} Q_l^{\,t}(\phi,\vartheta)}{\iint\limits_{A_j} F^{\,t}(\phi,\vartheta)}$$

Where A_j is the list-mode specific acceptance area. $Q_l(^t)$ is the radiance distribution for pixel l for the tth estimate, and $F^{(t)}$ is the total radiance distribution for the tth source estimate. The algorithm updates the estimate of the source distribution for each list-mode event. After a run through the list-mode data set, the emission radiance distribution is recalculated and used in the next iteration.
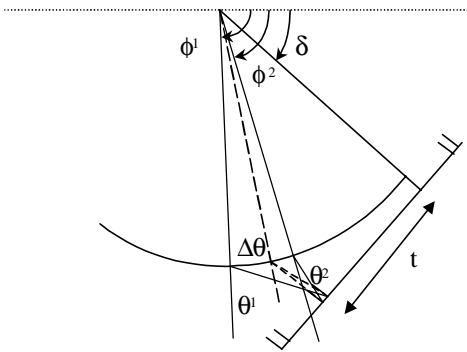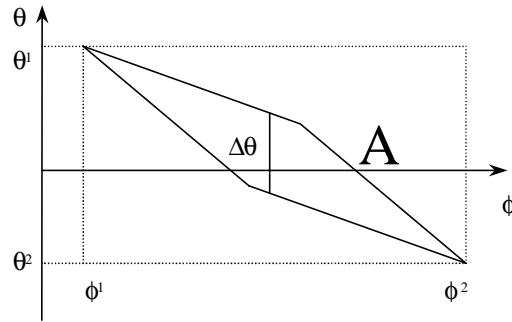

Fig.2.   Fig.3.

Results: Figure 4 shows the reconstructed images, together with their angular sinogram for a point source out of center, over three iterations.
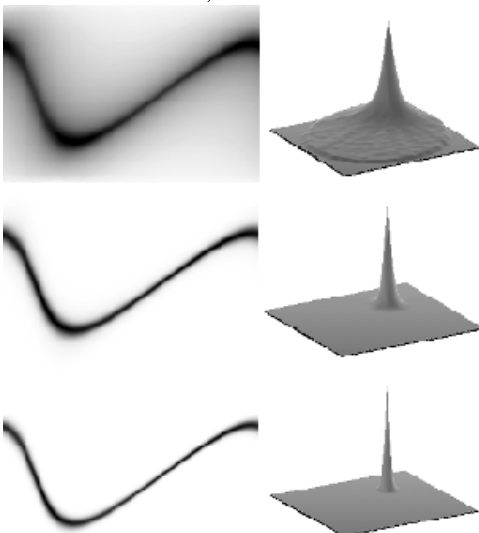

Fig.4.

Discussion and conclusion: The forward operator projecting the source distribution onto the intermediate stage is completely camera independent. The known hardware characteristics can be taken into account in the backprojection of the projection data. The calculation of the region $A(\phi,\theta)$ can be changed to a fan-beam, pin-hole or cone-beam collimator with minor adjustments.

We have developed a projector/backprojector pair, which uses an intermediate stage and an alternative ray representation. We showed the method can be applied to list mode reconstruction for SPECT.

Segmentation of hippocampus from MR images using geometric models

Jan Klemencic, M.Sc.[a], Prof. Vojko Valencic, Ph.D.[a], Nuška Pecaric, M.D.[b]
[b]Faculty of Electrical Engineering, University of Ljubljana, Slovenia
[b] Clinical Institute of Radiology, University Medical Centre,Ljubljana, Slovenia

Introduction: Hippocampus atrophy is related to various brain diseases (temporal lobe epilepsy, schizophrenia). Atrophy detection is often essential for correct surgical decisions [1]. In clinical praxis, atrophy is subjectively evaluated from coronal magnetic resonance (MR) cross-sections by a neuroradiologist. On the other hand, computer-based segmentation allows objective volume and shape measurements, and is also more sensitive to minor pathologies. To avoid tedious manual segmentation, a supporting algorithm is needed. Standard segmentation algorithms are inappropriate, due to the poor hippocampus visibility on MR (many discontinuous or false edges, high noise, low contrasts). We developed an effective algorithm, customised to badly defined objects. It is based on deformable contours and employs built-in geometric models.

Methods: Addressing discontinuous edges, we applied deformable contours. Their strength is in their ability to treat objects as full, connected units. However, they are highly sensitive to noise, low contrasts and false edges. We overcame these problems by developing a specialised version (based on [2]), capable of exploiting a priori shape knowledge by means of built-in geometric models. We gather this shape knowledge by a simple algorithm initialisation: before starting the algorithm, some key MR slices (called the 'reference slices') must be manually delineated. By setting these initialisation contours into 3D space, we obtain a rough representation of the hippocampus. The representation is built into the contour deformation algorithm as a geometric model. We further refined the algorithm by adding specific features (contour mass-centre and perimeter adjustments, edge force weighting).

The algorithm then follows the established principle: a contour travels through individual image slices, deforms on each one in turn to fit to the local edges, and simultaneously attempts to stay close to the built-in geometric model. The resulting contours are stacked, describing the full 3D object.
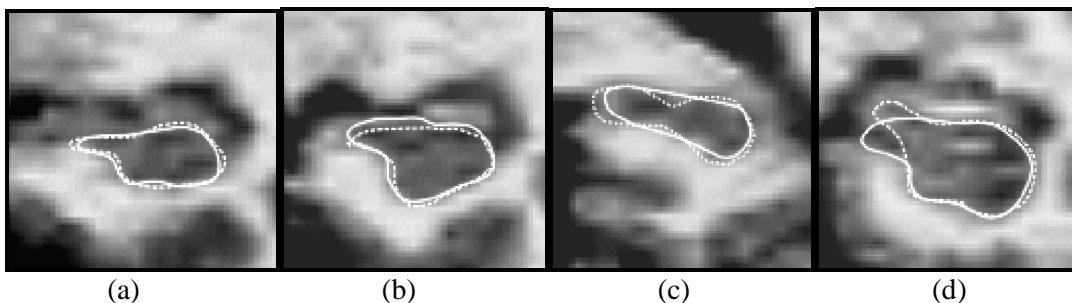

| (a) | (b) | (c) | (d) |

Figure 1: Exemplar results of automatic (full line) and manual (dotted line) segmentation.

Results: The algorithm was tested on 5 healthy and 3 atrophic hippocampi. Table 1 lists the results. The legends are: Vman-manual segmentation volume; Vaut-automatic segmentation volume; FPE/FNE-False Positive/Negative Error (voxels marked by algorithm, but not by manual segmentation, and vice versa); A_{agr}/A_{dis}-relative amounts of agreement/disagreement between Vman and Vaut.

Figure 1 shows some examples of algorithm results in comparison to manual segmentation. Figs.1(a-b) show a good match, while some mismatch remains on (c-d).

Hippoc.#	V_{aut} [cm^3]	V_{man} [cm^3]	V_{aut}/V_{man} [%]	FPE [%]	FNE [%]	A_{agr} [%]	A_{dis} [%]
1	2.623	2.577	1.8	9.1	6.8	92	18
2	2.597	2.549	1.9	8.4	5.9	93	17
3	2.235	2.240	-0.2	7.5	7.7	92	18
4	2.348	2.442	3.8	3.7	8.8	94	16
5	2.588	2.464	5.0	10.4	3.7	93	16
6	0.925	0.953	-2.9	8.7	12.6	89	25
7	1.010	1.027	-1.7	10.7	11.8	89	25
8	1.334	1.293	3.2	12.7	8.7	89	24

Table 1: Segmentation results. See main text for details.

Discussion: We used identical algorithm parameter values in all 8 cases, showing that the adjustment is only necessary once. During initialisation, we manually delineated approximately each fourth slice (on average), implying a 75% workload reduction. The fourth, shaded column in Table 1, shows a good match between manual and automatic segmentation. It falls within the range of usual manual segmentation errors. Also, a trained neuroradiologist found our segmentation results acceptable.

Columns 5-8 of Table 1 show various estimates of match between manual and automatic segmentations. These values may seem large, but manual segmentations by themselves also yield similar errors. This is mainly due to the low MR scan resolution. Hippocampus is a small structure, and removing a single layer of voxels from its surface can reduce its volume by 30% [3]. Consequently, high errors occur, even when the contours lie very close to the optimal position. Due to error averaging through the slice sequence, volume estimates remain accurate.

Each computation takes about two minutes on a 180MHz processor. This is acceptable, considering that 30-45 minutes is usually required for full manual segmentation.

References
[1] C.R. Jack, "Neuroimaging in Epilepsy", pp.111-119, Butterworth-Heinemann (1996).
[2] P. Radeva, J. Serrat, E. Marti, "A Snake for Model-Based Segmentation", Proc. 5.Int.Conf. Computer Vision, pp.816-821, Massachusetts (1995).
[3] T. Pfluger, S. Weil, S. Weis, C. Vollmar, D. Heiss, J. Egger, R. Scheck, K. Hahn, "Normative Volumetric Data of the Developing Hippocampus in Children Based on MRI", Epilepsia, 40(4); pp.414-423 (1999).

Skull smearing effect on event related potentials investigated with a resistor mesh model

X. Franceries, B. Doyon, N. Chauveau, B. Rigaud, J-P. Morucci and P. Celsis
INSERM Unit 455, Neurology Department, Purpan Hospital, Toulouse, France

Introduction: Neural activation results in event related potentials at the surface of the human scalp. Studies of the direct problem are usually achieved using models, including the three sphere model on the

one hand and numerical models on the other hand. The first one is the simplest and the only one that can give rise to an analytic solution. Numerical models, including BEM and FEM, are usually built from real head, making it possible to calculate scalp potential maps numerically. We propose here a new model, in which head tissues and stimulated neural activity are mimicked by a resistor mesh and an electrical current source plugged in between two nodes of the mesh. This model has been applied for studying the effects of skull conductivity anisotropy.

Method: Brain, skull and scalp can be represented by three concentric spheres of 72, 79 and 85 mm in radius, exhibiting conductivities of 0.33 S.m-1 for brain and scalp, and 0.0042 S.m-1 for the skull (isotropic model). These spheres were split into small volume elements. Each one was modelized by a resistor, whose value was calculated to reproduce the electrical properties of this volume element along the radial and both tangential directions of the spherical coordinate system. The mesh is composed of 43,102 resistors, connected to 14,123 nodes and arranged in 23 spheric layers. Each layer corresponds to equivalent tissue depth up to 4 mm. Angular sampling was 10 degrees. The potential at each node was calculated by a mixed-signal mixed-technology simulator (Saber), then voltage and current density mappings were obtained using a Matlab interpolation function. In view to investigate the effect of the anisotropic electrical properties of skull on scalp potential mapping, the skull tangential resistances have been changed, taking into account a tangential conductivity 10 times higher (anisotropic model).

The mesh model has been validated, for a given dipole, by comparing the solution of the direct problem obtained with the mesh model on the one hand and with the basic three shell model (analytic solution) on the other hand. Owing to the ability of the mesh model to provide the potential at any node, spatial potential and current density distributions on scalp and cortical surfaces have been compared.

Results and discussion: Comparison of data from the mesh model and those given by the analytic solution did not exhibit significant difference. Moreover, this mesh model provides similar results as FEM model exhibiting about the same number of elements [1]. Figure 1 shows an example of potential mapping, obtained with the isotropic model, on (a) scalp and (b) cortical surfaces, illustrating the strong smearing of spatial potentials after current has flowed through the skull. Figure 1c is a cross section that shows the plane where the dipole was simulated (pointer) and then gives an insight of the potential distribution in the head. This picture shows that the low conductivity of skull makes potential distribution shift slightly towards the sphere center.

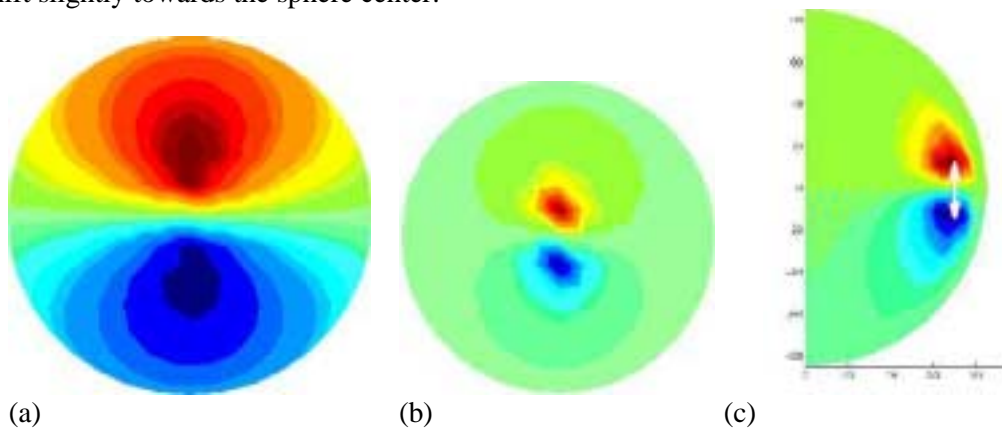(a)   (b)   (c)

Fig. 1: Example of potential mappings from the isotropic mesh model.
(a) Scalp potential; (b) Cortical surface potential; (c) Potential cross section of half the mesh in the plane where the current source was simulated (pointer).

Figure 2 presents scalp potential and current density maps obtained with the anisotropic model. It demonstrates that taking into account skull anisotropy results in a reduced maximum potential regarding the isotropic model. The current density mapping is not so much modified. These results illustrate the interest of cortical surface potential imaging [2] and scalp current density mapping [3]. As a matter of fact, their narrowed spatial distributions permit to improve the accuracy with which a dipole is localized. Besides, taking into account skull anisotropy is of prime importance to reduce dipole localization errors, particularly on the radial direction, when comparison is done with neural activation localisation in functional magnetic resonance imaging (fMRI).
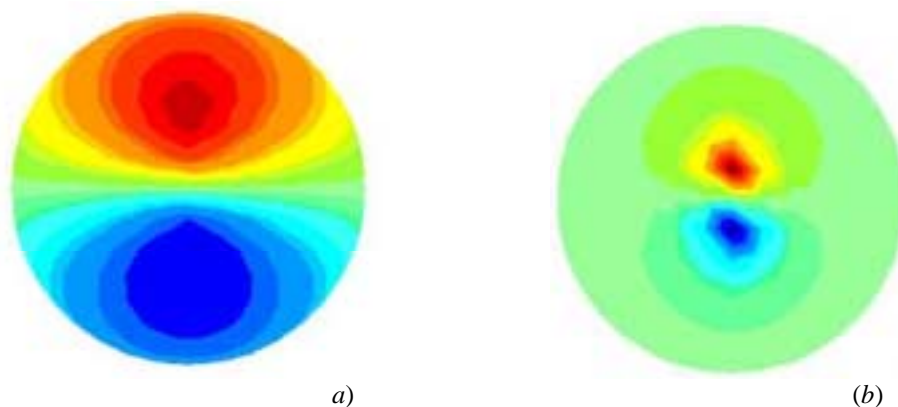

a)   *(b)*

Fig. 2: (a) Scalp potential and (b) current density maps from the anisotropic model in the same conditions as in fig. 1

References
[1]   G. Marin G., C. Guerin C., S. Baillet S., L. Garnero, G. Meunier, Human Brain Mapping 6: 250-269 (1998).
[2]   P.L. Nunez, Proc. SPIE, 1887: 22-39 (1993).
[3]   F. Perrin, O. Bertrand, J. Pernier, IEEE Trans. Biomed. Eng. BME34 : 283-288 (1987).

Three-dimensional geometric sensitivity correction in triple-headed gamma camera coincidence imaging: Separability properties

Yves D'Asseler, Stefaan Vandenberghe, Michel Koole, L. Bouwens, Rik Van de Walle, Ignace Lemahieu, Rudi A. Dierckx

Introduction: Gamma camera PET (Positron Emission Tomography) offers a low-cost alternative for dedicated PET scanners. However, sensitivity and count rate capabilities of dual-headed gamma cameras with PET capabilities are still limited compared to full-ring dedicated PET scanners. To improve the geometric sensitivity of these systems, triple-headed gamma camera PET has been proposed. As is the case for dual-headed PET, the sensitivity of this kind of devices varies with the position within the field of view (FOV) of the camera. This variation should be corrected for when reconstructing the images. In earlier work, we calculated the two-dimensional sensitivity variation for any triple-headed configuration. This can be used to correct the data if the acquisition is done using axial filters, which effectively limit the axial angle of incidence of the photons, comparable to 2D dedicated PET. More recently, these results were extended to a fully 3D calculation of the geometric sensitivity variation. In this work, the results of these calculations are compared to the standard approach to correct for 3D geometric sensitivity variation.

Methods: Current implementations of triple-headed gamma camera PET use two independent corrections to account for three-dimensional sensitivity variations: one in the transaxial direction and one in the axial direction. This approach implicitly assumes that the actual variation is separable in two independent components. We recently theoretically calculated the 3D sensitivity variation, and in this work we investigate the separability of our result.

To investigate the separability of the sensitivity variations, an axial and transaxial profile through the calculated variation was taken, and these two were multiplied, thus creating a separable function. If the variation were perfectly separable, this function would be identical to the calculated variation. As a measure of separability, we calculated the percentual deviation of the separable function to the original variation. Separability was investigated for three different detector configurations: a dual headed system, a triangular configuration and a U-shape configuration (Figure 1).

XX

Figure 1: Investigated Configurations.

Results: We investigated the separability for several camera configurations and rotation radii. We calculated the mean absolute percentual difference between the calculated and the separable sensitivity map. We found that, for all configurations, the variation is not separable , and becomes less separable as the rotation radius tends to smaller values. This indicates that in this case, our sensitivity correction will give better results than the separable correction now applied.

In figure 2. , the percentual difference is plotted as a function of detector radius for the whole FOV. The fact that the differences become larger for increasing detector radius is due to the fact that part of the outer bounds of the FOV are not included in the calculation because of physical restrictions of the camera. In this part, the differences are largest, and this plays a more important role for smaller radii.

In figure 3., the difference is plotted for the central 20 cm disc of the FOV. In this case, the aforementionned effect is not seen, since the FOV is the same for all detector radii. It then becomes clear that separability is better for configurations with larger radii.
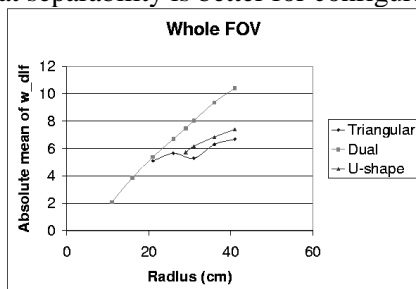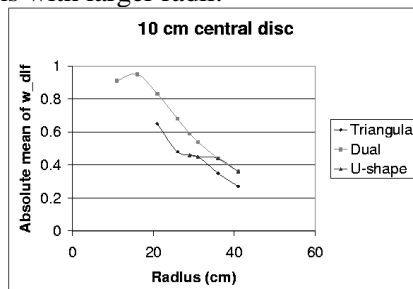

Figure 2   Figure 3

Discussion: The differences we found between the calculated sensitivity maps and the corresponding separable maps had a mean over the FOV of up to 10%, and reached maximum values of up to more than 50%. This indicates that the full three-dimensional calculation should be used for geometric sensitivity corrections in three-headed coincidence imaging.

References
[1] C. Matthews, "Triple-head coincidence imaging", in Conference Record of the 1999 IEEE Nuclear Science Symposium and Medical Imaging Conference, Vol 1, Seattle, USA; October 1999
[2] Y. D'Asseler, S. Vandenberghe, M. Koole, L. Bouwens, R. Van de Walle, R.A. Dierckx, I. Lemahieu, "Geometric Sensitivity Calculation of three-headed gamma camera-based coincidence imaging", presented at the SPIE Medical Imaging Conference 2000; pp 58-67, San Diego , USA; February 2000
[3] Y. D'Asseler, S. Vandenberghe, C. Matthews, M. Koole, R. Van de Walle, I. Lemahieu, R.A. Dierckx, "Three-dimensional geometric sensitivity calculation for three-headed coincidence imaging", in Conference Record of the 2000 IEEE Nuclear Science Symposium and Medical Imaging Conference, Vol 1, Lyon, France; October 2000

Correction for the varying detection efficiency in gamma camera based coincidence detection

S.Vandenberghe[a], Y.D'Asseler[a],R.Van De Walle[a], I.Lemahieu[a], R.A.Dierckx[b]
[a] *Ghent University, Department of Electronics and Information Systems, Sint Pietersnieuwstraat 41, B-9000 Ghent, Belgium*
[b] *Ghent University Hospital, Division of Nuclear Medicine , De Pintelaan 185, B-9000 Ghent, Belgium*

Introduction: Most gamma cameras used for PET imaging improve sensitivity by the use of thicker crystals. This increased thickness has some side effects. In single photon emission computed tomography the mechanical collimation only allows photons which are close to the perpendicular on the crystal. In PET imaging this mechanical collimation is replaced by electronic collimation. This implies that also coincidences with a large deviation from the perpendicular are detected which have a higher probability of being detected.

The result of this effect on the sensitivity is evaluated for different configurations. This is done by analytical calculations and Monte Carlo simulations. First the simulations were done in 2D. This is extended to 3D by taking the axial width of the crystal into account. Two correction methods are proposed for this image degradation. One of this is based on an LOR correction, while the other is voxel based.

Methods: To obtain the sensitivity for a LOR, it is necessary to know the 511 keV photo peak detection efficiency for different crystal thicknesses. This is obtained by making a second order fit to the values of a 511 keV photo peak efficiencies [1]. These values were varified by performing a Monte Carlo simulation (Geant) for different thicknesses. Photons were generated in a 0.1 degree emission cone. The crystal was placed in front of this cone and the ratio of detected photons to the emitted photons gave the sensitivity. This is shown in figure 1.

The coincidence detection efficiency is the product of each of the single photo peak efficiencies. Each single photo peak efficiency is obtained by the value of the sensitivity for a thickness calculated by taking the ratio of the original thickness divided by cos(, with (the angle with the perpendicular. To obtain the (crystal thickness corrected) sensitivity in a pixel the sensitivity of all possible coincidences through the pixel are backprojected. When assuming a constant sensitivity independent of the incident angle, the geometrical sensitivity is obtained.

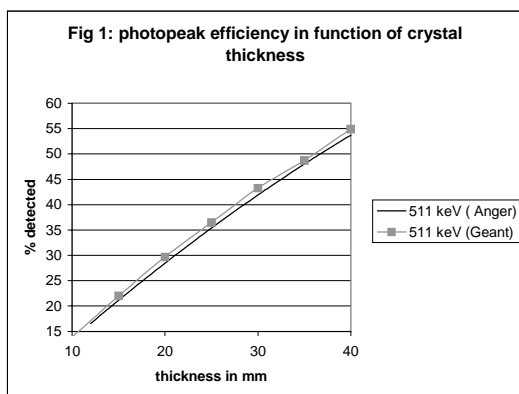**Fig 1: photopeak efficiency in function of crystal thickness**

Fig.1

This simulation was extended to 3D for a triple head configuration with heads at 0°, 90° and 270°. The ratio between the crystal thickness corrected sensitivity and the geometrical sensitivity is shown in Fig. 2. The highest variation in the radial direction is towards the edge of the FOV. It is clear that there is an axial variation as well. When looking in the axial direction (vertical cut) it is clear that the highest ratio is obtained in the axial center. The results of the simulations in 2D was similar to the horizontal profiles of Fig 2. Similar figures were obtained for a standard dual head configuration and a triangular triple head configuration. The variation was limited for a dual head configuration and less pronounced for the triangular configuration than for the Ushape configuration.
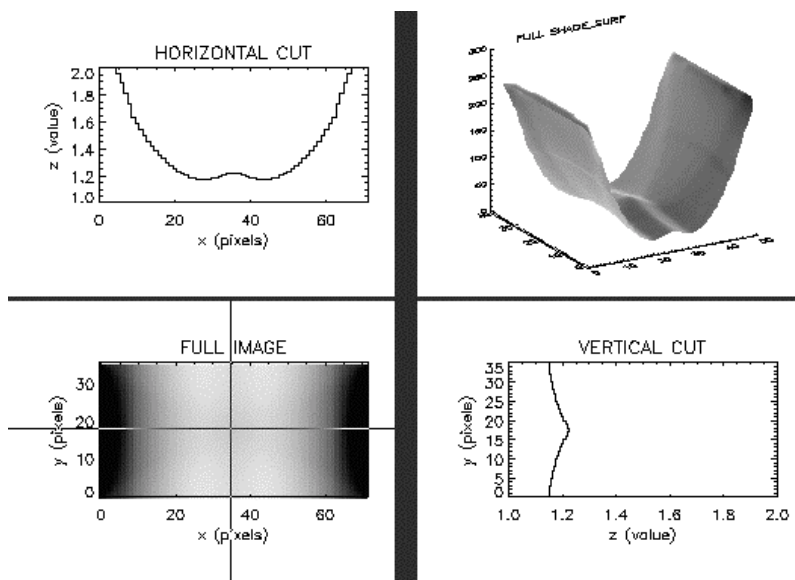
Fig.2

The results show that an appropriate correction is necessary. This is done by either weighting each line of response for its detection efficiency and geometric sensitivity before including it into the reconstruction or by dividing each pixel by a sensitivity factor after each iteration. The list mode data of a
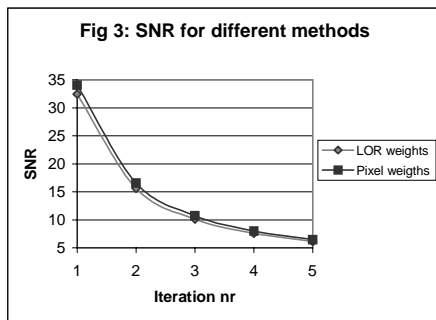
Fig 3: SNR for different methods

Fig.3

uniform phantom were reconstructed with both methods. As a measure for the signal to noise ratio, the mean in a circular region was divided by the standard deviation in the same region. The pixel based method results in a SNR which is a little bit higher than the other method. This is shown for different iteration numbers in Fig 3.

Conclusions: It is shown that there is an influence of the crystal thickness on the sensitivity profiles of triple head gamma camera systems. There is an limited axial and a more pronounced radial variation. The pixel based correction for this effects results in a slightly higher SNR than the LOR based method.

References

[1]   [1] Gamma ray efficiency and image resolution in Sodium Iodide,Anger, Rev. Sc. Instr. 1964
[2]   [2] Geant 3.21, Detector description and simulation tool, CERN Program Library Long Writeup W5013,CERN Geneva,Switzerland,1993

Session – Medical Imaging 2
Room 3, Thursday 3 May, 16.15 – 17.30

Multidimensional images of medical data by mathematical registration methods

W. Hauck[a], H.F. Zeilhofer[a,] Z. Krol[b], E. Keeve[b], R. Sader[a], K.-H. Hoffmann[b], C. Ganter[c], E. Rummeney[c], N.Avril[d], M. Schwaiger[c]
[a]*Department of Oral and Maxillofacial Surgery, University of Technology Munich/Germany*
[b]*Caesar - Center of Advanced European Studies and Research, Bonn, Germany*
[c] *Department of Radiology, University of Technology, Munich, Germany*
[d]*Department of Nuclearmedicine, University of Technology, Munich, Germany*

Introduction: Several diseases in the head and neck area require that different imaging modalities (CT, MRI, SPECT, PET and others) are applied in the same patient. These different investigation modalities have their specific advantages and disadvantages. The combination of different methods allows to make the best use of the advantageous properties of each method while minimizing the impact of its negative aspects: MRI imaging is the mean of choice to describe soft tissue alterations that may be unrecognizable in the relating CT. Bone tissue, on the other hand, is optimally imaged in CT. Inflammatory nuclei of the bone can be detected best by their increased uptake of radioisotopes detected in SPECT. Only the

combination of all modalities let the physician come to an exact statement on pathological processes that involve multiple tissue structures.

Methods: 24 patients with different complex diseases (malignant and benigne tumours and inflammatory diseases) were examined with CT, MRI, PET and SPECT of the head and neck area in correlated anatomical positions. The aim was a preoperative description of the exact dimension and dignity of the pathological process for planning porposes of the following surgical treatment. It was necessary to correlate the different investigation-datas with mathematical methods to create multimodal data sets. The several surfaces and voxel based matching functions we are using allow a precise merging by means of numerical optimization methods like e.g.simulated annealing without the complicated assertion of fiducial markers of the localization landmarks in two dimensional cross sectional slice images. The quality of the registration depends on the choice of the optimization procedure according to the complexity of the matching function landscape.

Results: The superimposition of morphological data (CT, MRI) with functional (SPECT, PET) data lead to new options in diagnosis and therapy. Tumors, inflammatory nuclei or vascular dysplasia can be localized more accurately through the combination of morphological and functional data (multimodal data sets) and can be differentiated better from healthy tissue structures. Besides the various 2D techniques to display fused slices, we have developed hybrid 3D visualization methods based on the volume and surface rendering techniques. Combining this with stereoscopic presentation and animation algorithms (rotation, cine-loops) significantly enhances the perceptions of three-dimensionality during the examination. We tested the method in 24 patients with various complex diseases. We present examples of hybrid images involving CT, MRI, SPECT and PET data sets (s.figure).

Discussion: The high technical, personal and financial impact is in relation to the aquirement of better preoperative surgical planning, which reduces the operation time and leeds to more sophistic concepts. Even it is possible to give the patient an idea of his medical treatment and suspected postoperative result.

In the nearer future it will be possible to use multimodal data sets as a possibility for intraoperative navigation and planning in the reconstructive surgery.
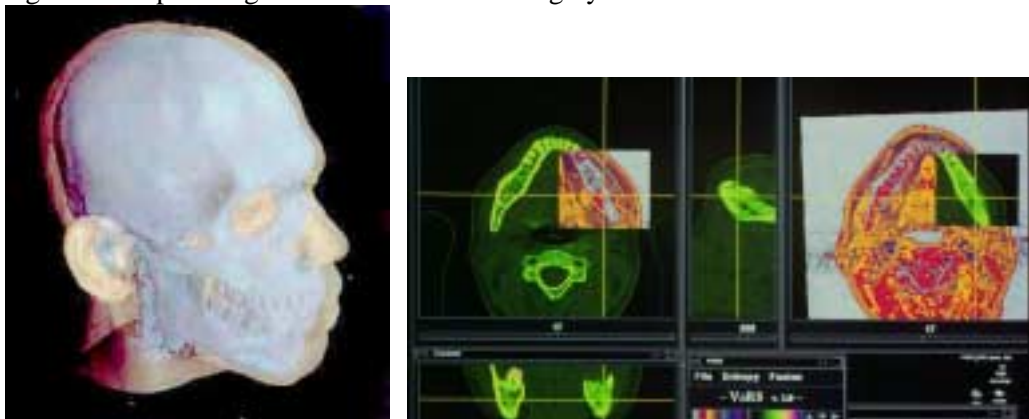
Multimodal dataset of CT and MRI   Visualisation of the 2 modalities in the multimodal dataset

Conclusion: Precise correlation of the multimodal images of the head and neck area combined with its 2D- and 3D-representation techniques provides a valuable tool for physicians. Thus, the patient benefits from improved diagnostics an consecutive therapy. Future will be to use this datasets for properative

simulation, planning and intraoperative navigation. The first results of this work in progress will be presented as well.

References

[1] Zeilhofer H.-F., Król Z., Sader R., Hoffmann K.-H., Gerhardt P., Schweiger M., Horch, H.-H.: Diagnostic possibilities with multidimensional images in head and neck area using efficient registration and visualization methods. In: Image Display Proc. SPIE Vol. 3033, 1997, 124-131

[2] Zeilhofer H.-F., Król Z., Sader R., Hoffmann K.-H., Hogg M., Schwaiger M., Gerhardt P., Horch H.-H.: Multimodal Images in Diagnostics of Head and Neck Area Using Efficient Registration and Visualization Methods. In: Lemke H.U., Vannier M.W., Inamura K. (Eds): Computer Assisted Radiology and Surgery, Elsevier Amsterdam Lausanne New York Oxford Shannon Tokyo, 1997, 723-728

Address for correspondence: Dr.med. Wolfgang Hauck, Department of Oral and Maxillofacial Surgery, University of Technology, Ismaninger Str. 22, D-81675 Munich, Germany.
Tel.:   +49-89-4140-2932; Fax: +49-89-4140-2934;Email: wha@mkg.med.tu-muenchen.de.

Detection of glutathione in the human brain in vivo by means of double quantum coherence magnetic resonance spectroscopy

D. Meier, U. Dydak, P. Boesiger
Institute of Biomedical Engineering, University and ETH Zurich, Switzerland

Introduction: Localized proton magnetic resonance spectroscopy (1H MRS) allows for non invasive observation of cell metabolites in specified regions of the human brain in vivo. One interesting metabolite is Glutathione (GSH) which plays an important role for many neurological diseases, e.g. schizophrenia or epilepsy.

The changes in GSH concentrations in CSF might be a direct or indirect reflection of changes in brain areas involved in the pathophysiology of schizophrenia. To monitor non-invasively GSH levels in the human brain tissue new 1H Magnetic Resonance Spectroscopy techniques were developed that allow detection of GSH with a high selectivity. In conventional 1H MR spectra GSH is not visible due to its rather low concentration, its complicated spectral pattern and spectral overlapping with other resonance lines.

Methods: We use a double quantum coherence (DQC) filtering sequence in combination with PRESS volume selection (Fig. 1). The strongly coupled cysteine CH2 compound of GSH (multiplet at 2.9 ppm) was found to be the most suitable target for spectral editing

The double quantum filter technique provides excellent background discrimination between the cysteine compound of GSH and the uncoupled creatine spins. A non-neglectable fraction of signal from aspartate leaks through the filter. In vitro experiments showed that the spectral resolution is sufficient to separate GSH and aspartate signal on the basis of the differences in their chemical shifts. A minor contribution to the observed signal originates from GABA, which is neglectable for the poor yield in combination with the low concentration of GABA.
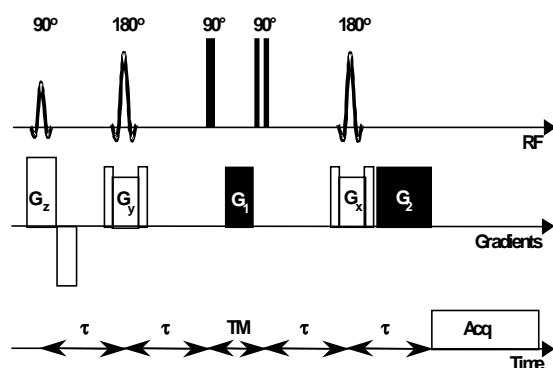
Figure. 1: .DQC filtering sequence. G1 = 10 mT/m · 3 ms, G2 = 2G1; ? = 18.75 ms, TM = 9 ms. The third 90° pulse, which converts DQC into antiphase magnetization, is made frequency selective, such that it only affects the ω proton of cysteine, but not its CH2 compound.

Results: In vitro tests show that the DQC filtering method provides good discrimination between the GSH signal at 2.9 ppm arising from the cysteine CH2 compound and the interfering resonances of (aminobutyric acid (GABA), creatine (both at 3.0 ppm) and aspartate (at 2.8 ppm). Fig. 2 displays a representative in vivo DQC filtered spectrum. In the in vivo measurements a mean ratio of GSH signal to tissue water signal of $(5.7 \pm 2.3)x$ $(10^{-5}$ (range: $2.9x10^{-5}$ - $9.3x10^{-5})$ was found. No gender dependence of the ratio GSH/water was found. Estimations gave an average GSH concentration in the range of 2-4 mmol/l for healthy volunteers, in keeping with biochemical measurements assuming intracellular concentrations of 1 - 10 mmol/l.
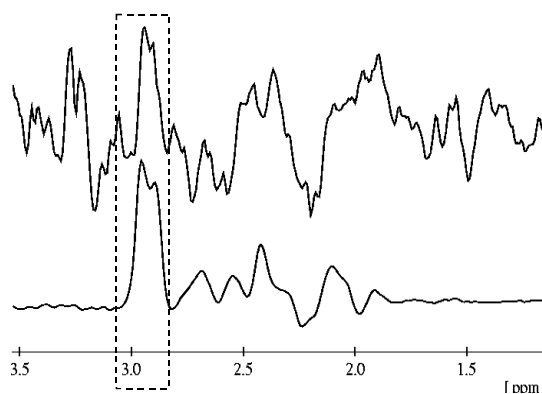
Figure 2. Bottom: In vitro DQC filtered spectrum of pure GSH. Top: Typical in vivo DQC filtered spectrum. The characteristic resonance at 2.9 ppm was visible in the DQC filtered spectrum of all 12 subjec

MR study: In the control group a mean GSH signal/water signal ratio of $(5.6 \pm 2.6)x10^{-5}$ was observed in the prefrontal cortex. In schizophrenics we found a mean GSH signal/water signal ratio of $(2.9 \pm 1.6)x10^{-5}$ (Fig. 3). The GSH level was thus decreased by ~50% in the patients compared to controls ($p<0.02$; Mann-Whitney test). Estimations gave an average GSH concentration in the range of 2-4mM for the control group, in keeping with biochemical measurements in ex vivo samples. No significant change

was seen in Cre and Cho levels. NAA concentrations, however, were 31% (p=0.0012; Mann-Whitney test) lower in schizophrenics (6.0±1.1mM; n=8) than in controls (8.7±1.4mM; n=10). This is consistent with the NAA decrease reported in frontal lobe of schizophrenics.

In the CSF samples GSH was decreased by 42% (p<0.05; ANCOVA) in the patients (327 ± 127 pmol/ml) compared to the control subjects (565 ± 508 pmol/ml).
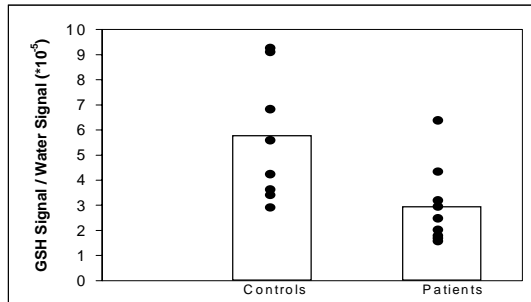
Figure 3

GSH levels in schizophrenic patients as measured by 1H spectral editing MRS in medial prefrontal cortex are significantly lower than in healthy volunteers (p<0.02, Mann-Whitney test). Displayed are the mean values ± standard deviation (box) and all individual values.

Study of the quantification of fbp ect images with a correction for partial volume effects

M. Koole[a], R. Van de Walle[a], K. Van Laere[b],Y. D'Asseler[a], S. Vandenberghe[a], L.R. Bouwens[a], I. Lemahieu[a], R.A. Dierckx[b]
[a]*Ghent University, Department of Electronics and Information Systems, Sint Pietersnieuwstraat 41, B-9000 Ghent, Belgium*
[b]*Ghent University Hospital, Division of Nuclear Medicine, De Pintelaan 185, B-9000 Ghent, Belgium*

Introduction: ECT images provide in vivo quantitative measurements of physiological, biochemical or pharmacological processes. Because of the limited resolution of ECT, partial volume effects (PVE) obscure the accurate interpretation of ECT data. Extensive research has already been done for the quantification of brain ECT images. Two methods were proposed allowing simultaneous estimation of the activity in a larger number of VOIs, still assuming constant activity throughout a VOI. One method takes into account the whole ECT image [1], while for the other method a sufficient number of VOIs have to be delineated on the reconstructed ECT image [2]. This paper compares the two methodologies.

Methods: The formalism for the ROI approach is:

$$A_j^{ROI} = \frac{1}{n_j^{vox}} \sum_{i=1}^{N} A_i \int_{ROI_j} \left(\int_{D_i} h(r,r')dr' \right) dr$$

with A_j^{ROI} the average activity calculated over a delineated ROI_i within the reconstructed ECT image with n_j^{vox} number of voxels, N the number of functionally different tissue com-ponents, each of which has a constant real activity concentration A_i, and each one being defined over the spatial area D_i in the FOV, and $h(r)$ the appropriate point spread function as the response function of the detection system. In matrix notation, this set of equations can be written as $A^{ROI} = HA$ with

$$H_{ij} = \frac{1}{n_j^{vox}} \int_{ROI_j} \left(\int_{D_i} h(r,r') dr' \right) dr$$

The advantage of this approach is that only a relatively small square matrix has to be inverted in order to reconstruct the desired image. The size of this matrix depends on the number of modeled tissue components. The disadvantage is that the ROIs can be chosen arbitrarily and this choice will probably influence the result.

The formalism for the global image approach is the same, except that every pixel is considered as a ROI. The matrix notation becomes $B = HA$ with B the whole reconstructed ECT image and the i-th column of H is formed by the spatial area D_i over which the i-th tissue component is defined. The advantage of this approach is that is not ROI-dependent. The disadvantages on the other hand are the computational and storage requirements for a SVD of a large non-square matrix.

Results: We tested the methodologies described above by means of a two-compartment software phantom, containing one background compartment and one small central compartment. Activity values were attributed to the two compartments, resulting in a hot area, surrounded by inhomogeneous background activity, with a local hot area to background ratio of 1.5 and a global hot area to background ratio of 1.2, considering the total background activity. A SPECT study was simulated by

a   b   c

d   e   f.
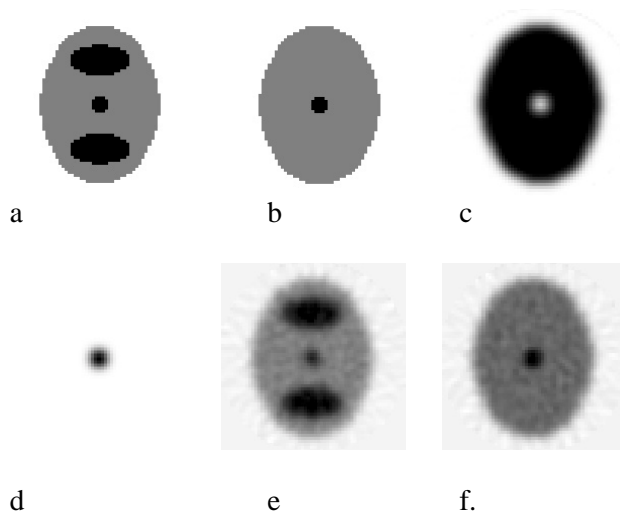
Overview of the simulated test images.

means of forward projecting the phantom, taking into account the distance dependent blurring of a parallel hole collimator (scatter and attenuation were not included). Poisson noise was added to the sinogram and the reconstruction was done by filtered backprojection. The same was done for the so-called region maps, except for adding the noise after the project step, so that the region maps were compliant with the resolution in the ECT image.

For the ROI approach two regions were chosen so that the matrix is easily invertible, that is a region containing only the background compartment and a region containing the small compartment and the background compartment. In this case the matrix becomes an upper or lower diagonal matrix and the solution of the set of equations is easily found by backsubstition. This approach was already followed for studying the quantification of tracer uptake in the basal ganglia by means of hardware phantom studies [3].

For the global image approach, we used the SVD to obtain the pseudo inverse of the matrix, which yields the minimum norm least square solution of the set of equations.

Testing the two approaches with the simulation study, shows an underestimation of the activity in the small compartment, due to an overestimation of the background activity, near the small compartment. However, the underestimation error is larger for the ROI approach (calculated hot area to background ratio of 0.6) than for the global image approach (calculated hot area to background ratio of 0.96).

Discussion: We compared two methodologies, a ROI approach and a global image approach, for quantifying an ECT image, taking into account PVE. We found the latter more performant than the former.

References
[1] C. Labbé, M. Koepp, J. Ashburner, T. Spinks, M. Richardson, J. Duncan, V. Cunningham, 'Absolute PET quantification with correction for partial volume effects within cerebral structures', Quantitative Functional Brain Imaging with Positron Emission Tomography, Academic Press, 1998; Chapter 9; 59-66.
[2] OG. Rousset, Y. Ma, AC. Evans, 'Corrections for partial volume effects in PET: principle and validation', J. Nucl. Med. 1998; 39; 5:904-911.
[3] M. Koole et al., 'MRI-guided quantification of SPECT images of the basal ganglia: a phantom study', accepted as poster presentation, WC on Medical Physics and Biomedical Engineering, July 2000, Chicago, USA.

An interpolation of RI image by means of 2D interpolating digital filter

J. P. Kowalski
Chair of Signal Processing and Multimedia Engineering,Technical University of Szczecin, Poland

Introduction: A radioisotope medical examination affords an information about metabolism. A radioisotope (RI) picture has lower resolution than X-ray picture. The X-ray picture may be an exact map, on which the transparent RI image is coating on, for specify a precise place of an unnormal metabolism. The coating of these two pictures requires their mutual size adjustment. That size adjustment is obtained by the interpolation. In the contribution the method of RI image interpolation by means of 2D digital filter is described.

Methods: An RI picture is a matrix of pixels. These pixels are data points. 2D digital filter is an implementation of the algorithm converting input data file - the RI image with an initial resolution - into output file - the required resolution RI image. The algorithm is based on Z-transform.

Results: An implementation of Z-transform is a simple method of synthesis and design of an interpolation algorithm. The file of the coefficients - the weights of 2D digital filter - is univocally specified and depends only from the number of data points used for interpolation.

Discussion: The described method allows easy interpolation of 2D image. The change of the number of pixels used for interpolation needs repeated computing of weights of 2D filter but by the same simple method.

References
[1] A. Wojtkiewicz Elementy syntezy filtrow cyfrowych WNT Warszawa 1984
[2] Z. Fortuna, B. Macukow. J. Wasowski Metody numeryczne WNT Warszawa 1998

# Image processing in artificial human vision systems

Justin Boyle, Anthony Maeder, Wageeh Boles
School of Electrical and Electronic Systems Engineering
Queensland University of Technology, Brisbane, Australia

Introduction: Several international research teams are currently developing artificial human vision ("bionic eye") systems that have the potential to restore some visual faculties to blind persons [1-2]. The approaches adapted by the various research teams range from retinal, optic nerve and cortical stimulation. However a common element is that they require a system that converts a visual scene into electronic pulses that stimulate nerve cells in the visual pathway (via implanted electrodes). It is anticipated that this stimulation induces a crude "image" in the visual regions of the brain. The usefulness of the induced image is dependent on how much visual information is presented, which in turn is determined by image quality and image processing.

Conclusions on image quality cannot yet been drawn, as in-vivo human trialing of visual prostheses has not been extensive. While it is likely that higher numbers of implant electrodes would result in higher spatial resolution of images (and hence higher quality images), size and manufacturing constraints limit electrode numbers in implants. Our research is based on optimising the amount of useful information obtainable from the relatively few electrodes by using image processing techniques.

Method: We have undertaken psychophysical testing on possible operating modes for an artificial vision system, to identify the most informative image processing operations which lead to better understanding of picture content. These processing operations include varying spatial resolution, brightness and contrast, extracting edges, mapping distance to image intensity and mapping "important" image regions to intensity.

Our experiments were aimed to quantify the performance of various image processing techniques in improving scene recognition and understanding. This assessment was achieved by presenting degraded images to 174 normally sighted viewers and asking them to identify the scene and make use of the data. The emphasis was on recognition for mobility purposes and obstacle avoidance. Participants were drawn on a voluntary basis and had no prior knowledge of the nature of the images. The images were processed to extract importance features, or close features, or edges etc. and then 'degraded' to low spatial resolution and low grey-scale images. A phosphene mask was applied to each image to create the illusion of induced phosphenes (ie. pixels were circular and did not touch each other along their borders). An example of the image processing techniques used in the testing is shown below in Figure 1.
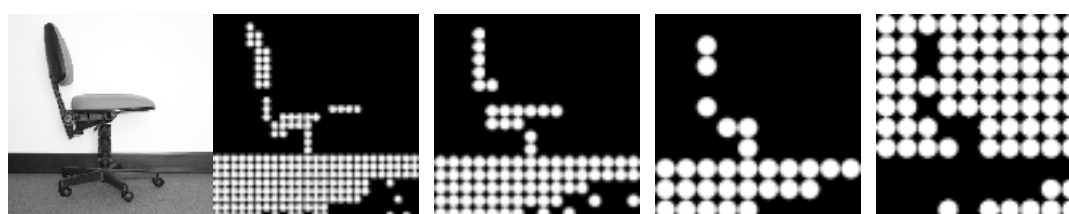
| Original | 25 x 25 | 16 x 16 | 10 x 10 | Inverse |

Spatial Resolution

3 grey levels	Edges	Distance Mapping	Importance' Mapping
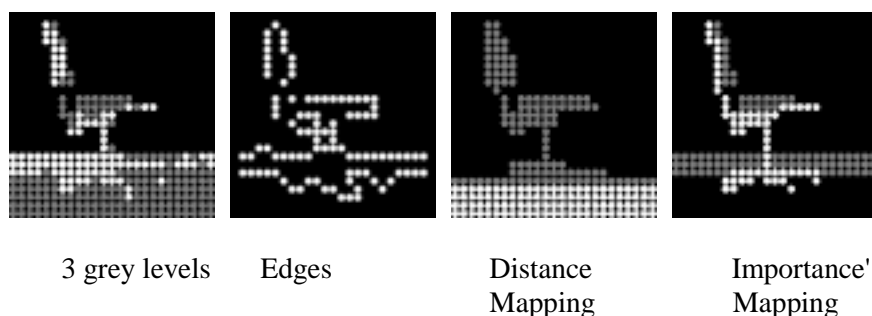
Figure 1: Image Processing techniques used in the psychophysical testing

Results:

* At a particular resolution, images with 3 grey levels (white, grey, black) are more recogniseable than black and white images.

* A higher resolution black and white image was more recogniseable than a lower resolution image with 3 grey levels. This indicates higher recognition is achieved with increased resolution rather than increased grey scale.

* The most recogniseable objects were human faces with 98% recognition.

* Several presentation modes should be used in artificial vision systems rather than a single mode of operation.

Discussion: Artificial vision research is steadily progressing, and medium-scale implantation of safe and useful prostheses may occur soon, perhaps in the next 2 - 4 years. In the designs under development, electrode numbers are limited, and there is a need to efficiently use the electrodes and corresponding phosphenes in the brain. It is thus timely to suggest means of increasing the information content of artificial vision systems. Our research ideas, using importance mapping, brightness modulation, range indication, and the delivery of supplementary information, will assist in providing visual information comparable to a normally functioning human eye but at far lower information rates. The basis of any successful artificial vision system will be such informative presentation of images.

References
[1]   Suaning G, Lovell N, Schindhelm K, Coroneo M, The bionic eye (electronic visual prosthesis): A review, Australian and New Zealand Journal of Ophthalmology 26, 195-202, 1998
[2]   Boyle J, Maeder A, Boles W, Digital Imaging Challenges for Artificial Human Vision, South African Computer Journal (26), pp.222-227, 2000

Session – Cardiovascular System
Room 3, Friday 4 May, 09.00 – 10.30

Multi layer perceptron for the prediction of ventricular repolarisation in function of the changes of heart rate

R. El Dajani[a,b], M. Miquel[a,b], M.C. Forlini[b], P. Maison-Blanche[c] , J. Fayn[b] and P. Rubel[a,b]
[a]Institut National des Sciences Appliquées de Lyon (INSA), Laboratoire D'Ingénierie des Systèmes d'Information (LISI), Lyon, France

[b]*INSERM XR121, Lyon, France*
[c]*Hopital Lariboisiere, Paris, France*

Introduction: Physiological signals are usually patient specific, and they are difficult to predict, especially for the cardiovascular system. New methods capable to be adapted to each case and to learn the singular behavior of heart functions should be developed to support physicians in their decision-making. One of the most widely studied relation is the QT-RR one, between the total duration of the ventricle activation and inactivation, and the heart rate [1]. Predictive modelling to the QT dynamic behaviour using RR may be a very precious diagnosis tool. The conception of such models would allow detecting life-threatening variations of the QT duration by comparing the predicted value to the real measured one [2]. In this paper we propose to model the QT dynamic behaviour in function of the history of RR intervals by means of a Multi Layer Perceptron (MLP). The networks will learn the following non-linear patient specific relationship: $QT_i = f(RR_i, RR_{i-1}, ..., RR_{i-M+1}, RR_{i-M})$ (1) where M is a time delay.

Methods: The complexity of physiological signals makes difficult to finalize and to validate the predictive models. Therefore we will also use, in addition to real data, simulated data for the design of the MLP and the assessment of their performances. For the modelling of the QT dynamics we have chosen an MLP architecture with 120 entries (i.e. time delay M of 4 minutes), 10 sigmoidal hidden neurons and one linear output neuron. Two neural models were created, the CC model learned on a night sequence recorded at 04:25 and belonging to a non-pathological 22 years old female (CLAV). The second model, GD, learned on a night sequence recorded at 05:54 and belonging to a non-pathological 27 years old female (GARD). The CC and GD models are then tested on the artificial data and on night ECG sequences belonging to the two patients, CLAV and GARD.

The standard deviation of the prediction error is used in addition to visual inspection to determine the match between the dynamic behaviour of measured QT and the predicted one.

Results: From figure 1, it can be noticed that the step response predicted by the MLP is very close to a first order step response for QT varying from 380 msec to 520 msec. Figure 2 shows the prediction result of the CC model on the RR CLAV sequence recorded at 07:35. The upper tracing of Figure 2-b corresponds to the measured QT interval (QTm) and the lower to the QT predicted by the MLP (QTp). The dynamic behaviour of QTp follows closely the real QT variations, with a standard deviation of the prediction error of 3.5 msec. The vertical shift between the two signals is due to a different time recording and to different activities of the sympathic and parasympathic systems. Both models give almost the same result with similar prediction error when applied on the CLAV sequences recorded between 02:23 and 07:35

Discussion: Although preliminary, our results indicate that Multi-Layer Perceptrons are able to approach the non-linear aspects of the QT-RR relationship, and can model both the dynamic behavior (response to a step impulse) and the steady state dynamic behavior (response to different, fixed RR intervals). The results obtained allow us to hypothesize that a "night prediction model" could be found. Further studies should be carried out to determine the influence of gender, age and the time of the day on the prediction quality.

References
[1]   SS. Chugh , K.L Kelly,JL Titus . *Circulation* 2000:102 pp. 649-54.
[2]   ML Fagundes, IG Maia, FE Cruz , PA Alves. *Arq Bras Cardiol* 2000: 75(2) pp. 115-24.
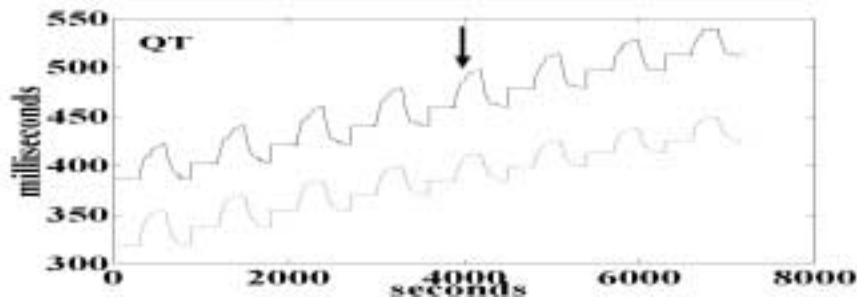
Fig. 1: - Result of real model prediction on the set of artificial data. The simulated signal is in dotted line and the ANN answer is in solid line. The arrow indicates the range of QT duration used for training.
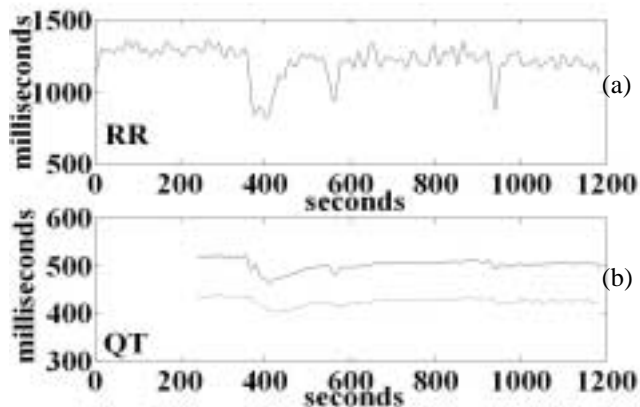
Fig. 2: *Real RR and QT sequences (in full line) and the predicted QT (in dotted line) produced by the MLP.*

Non-invasive analysis of haemodynamics in adolescents at rest and during exercise

Koen Matthys[a] Patrick Segers[a], Henri Verhaaren[b], Pascal Verdonck[a]
[a]*Institute Biomedical Technology, Ghent University (RUG), Belgium*
[b]*Paediatrics Department, Ghent University Hospital, Belgium*

*Introduction:*The analysis of the cardiovascular system at early age has an increasing social interest. Over the years, a lot of attention has been paid to the assessment of causes of atheromatosis (blood vessel degeneration). Several risk factors were clearly delineated, such as lack of physical exercise, smoking, diabetes. Methods that can identify people at risk - in a stage before the pathological process causes irreversible damage – are important from prevention point of view.

We the aim to improve early diagnosis, we are developing a set-up for the adequate haemodynamical analysis of heart function and arterial circulation properties by using arterial tonometry and Doppler ultrasound techniques. These non-invasive techniques are comfortable for the examined subjects and allow routine application.

The subjects are adolescents because (i) the grow factor is less dominant compared to young children, and (ii) the effects of the clinical pathology are not yet present, so that observations of risk factor repercussion are not interfered by any pathological damage.

Methods: A quantitative approach of the haemodynamics of heart and blood vessels is possible by calculation of mechanical parameters such as peripheral resistance (ratio of arterial pressure and cardiac output), arterial compliance (ratio of vessel volume variation and pressure variation), etc.[1]

Calculation of these parameters can be done on-line when three signals are simultaneously available: heart rate, aortic blood pressure and flow. Today however, these signals are mostly measured separately which is an important limitation for accurate basic haemodynamical studies.

With currently available non-invasive diagnostic tools (echo- and Doppler technology), it is possible to obtain cardiac flow wave patterns. On the other hand, conventional blood pressure measuring devices still do not apply continuous registration. A fairly new technology - tonometry -, however, allows continuous registration of blood pressure waveform. Pressures are measured non-invasively at a peripheral superficial artery (e.g. radial artery), and central aortic pressure is then calculated using a mathematical transformation with a (generalised) transfer function. It is however unclear whether this mathematical transformation, available for adults and in resting conditions, also applies to adolescents and during exercise.

Our goal is to develop a diagnostic set-up which essentially combines the continuous measurement of pressure and velocity wave morphology to derive a set of haemodynamical parameters, to be utilised in rest or during exercise tests. The three time-varying signals (ECG (heart rate), tonometrical signal (pressure) and Doppler signal (flow)) will be visualised on-line and derived haemodynamic parameters characterising the cardiovascular system will be calculated automatically.

A sensitivity analysis will reveal the impact of contact pressure, positioning of the pressure sensor and patient movement, on the accuracy of the registered blood pressure wave with the tonometer.

Also, a mathematical transmission-line-model, representing the aorta-radial path, will be further explored in order to compare two different methods of radial-to-aorta pressure transformation: (i) the classical Fourier transform and (ii) the autoregressive exogenous (ARX) model.[2]

Fig. 1. left: pen-type tonometer [Millar Instruments Inc.] middle & right: simultaneous registration of radial blood pressure and central aortic flow has already been realised during low stress activity.

Our findings will be validated in vitro in a cardiovascular simulator, as well as in vivo at the exercise laboratory of the Paediatric Cardiology Department (Ghent University Hospital). We will investigate the influence of smoking, physical exercise and diabetics on haemodynamical parameters in adolescents.

Conclusion: This work will contribute to the early diagnosis of people at cardiovascular risk. It will supply deeper insights on the effects of physical exercise, smoking and diabetes on the properties of the arterial system. The developed set-up can be used for on-line analysis during a conventional stress test without significantly prolonging the test protocol.

References
[1]   Nichols WW, O'Rourke MF. Mc Donald's blood flow in arteries. Theorethical, experimental and clinical principles. Third Edition ed. London: Edward Arnolds; 1990.
[2]   Fetics B, Nevo E, Chen C-H, Kass DA. Parametric model derivation of transfer function for noninvasive estimation of aortic pressure by radial tonometry. IEEE Transactions on Biomedcial Engineering 1999;46:698-706.

The deformation of arterial wall incurred by pulsatile flow (mechanical study – in vitro)

David Leitermann[a], Lubomír Poušek[b], Petr Volhejn[b], Michal Tota[a], Svatava Konvicková[a]
[a]*Czech Technical University in Prague, Faculty of Mechanical Engineering, Czech Republic*
E-mail: leiterma@fsid.cvut.cz
[b]*Czech Technical University in Prague, Centrum of Biomedical Engineering, Czech Republic*

Introduction: Mechanical studies of the pulsatile flow in the artery are of interest because of the influence of the vascular wall. The knowledge of arterial properties are the useful contribution for the description of development and progress of the arterial diseases. The expression of looked for conclusions is always conditioned by the obtained basic output data which are the only inputs for the calculation of the arterial properties. The measured magnitudes depend on the specific method. Lots of techniques were proposed and experiments were performed for the determination of the blood vessel elasticity, some based on the measurement of speedy vessel diameter and blood pressure over the cardiac cycle, others determining the propagation velocity of the pressure or volume wave along the vessel. This paper is focused on the experimental mock-line and the process of finding out the input data. These fundamental data are used for the determination of the pulse wave dispersion velocity. The possibility of the comparison of obtained data from described method and the magnetic resonance imagining (MRI) will be discussed.

Methods: The purpose of this work was to innovate an experimental mock-line and suggest a suitable noncontacting method to scan vessel wall deformation. The created mock-line is employed to simulate quantifiable and repeatable pulsatile flow through excised vessel under controlled hemodynamic condition (Fig.1). The distribution of the pulse wave was find out from the obtained pressure records. The aorta was fastened on the rigid plugs inside the housing chamber. The pressure transducers were installed in the plugs, i.e. close before and close behind. They allowed the scanning of speedy pressure values. The mutual shift of the records was the major information for the pulse wave progress. The effect of

individual flow parameters upon the arterial wall mechanics could be derived from simultaneous dynamic measurements of these parameters and changes in vessel diameter.
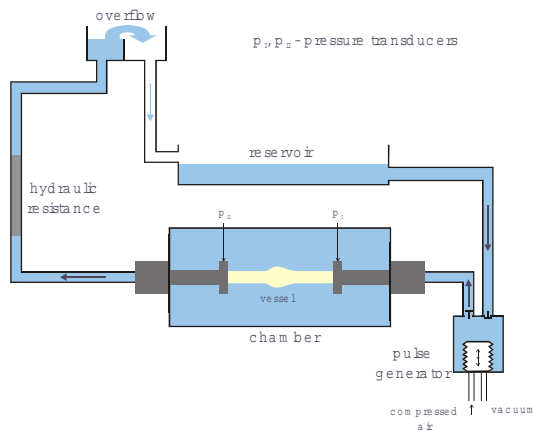
Fig. 1: The experimental mock-line.
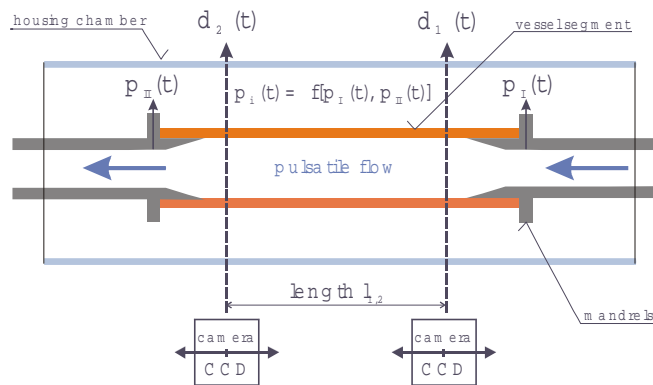
Fig. 2: The optical system of mock-line.

On the basis of scanning vessel wall movement we can determine pulse wave velocity in the vessel segment and also the relationship between external diameter and internal pressure (hysteresis loops). Hysteresis loops are the basic characteristic for description of nonlinear hyperelastic material such as vessel wall material. The mock-line was innovated by the installing of the optical system for the scanning the vessel wall movement (Fig. 2). The main elements of the used optical system were two 1-line scanning CCD cameras DALSA CL-P1 2048 equipped by photographical macroobjective SIGMA 105mm. CCD camera consists of array 2048x1 pixels with the edge size 10^{-6}m. The great advantage of this kind of camera was its scan-frequency (max. 23 kHz). The value of 10 kHz was adjusted for this experiment. The high level of incident light's intensity was important because of the clear record (picture). Therefore the artery was illuminated by thin laser beam. The pencil's shape was elliptic profile with the main axis approximately 40mm x 1mm. This was the reason of the satisfactory intensity of the laser diode by the power of 5mW.

Results: Several aorta segments were tested in this mockline in the preliminary study. The records from CCD cameras were obtained (Fig. 3). This method of determination of the arterial deformation was selected because of the similarity result's output as magnetic resonance also (Fig.4).
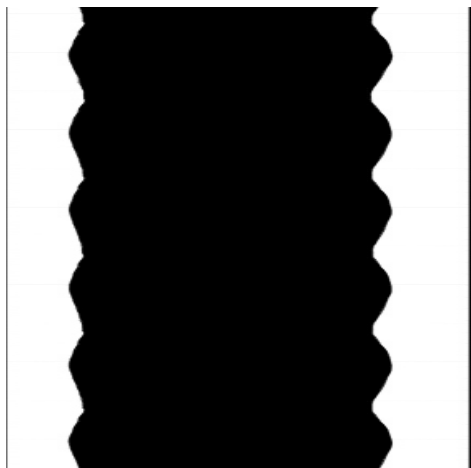
Fig. 3: The diameter record scanned by CCD camera.

Fig. 4: MRI output – diameter distribution.

Discussion: The comparisons of these outputs are next aim of the study. The relationship between the mechanical properties of the arterial wall and the arterial diseases (atherosclerosis, aneurism, hyperplasia, hypertension,…) as well as the dependence on the hemodynamic magnitudes of the pulsatile flow (pressure, heart frequency,…) will be investigate. Experiment data will be used for finding of the pulse wave velocity and results would be presented at the conference.

References
[1]   B.D. Bolster et al.: Accuracy of Arterial Pulse-Wave Velocity Measurement Using MR, JMRI 1997, Volume 8, Number 4.
[2]   K. Hayashi, K Ide, T. Matsumoto: Aortic Wall in Atherosclerotic Rabbits – Mechanical Study. JBE, Transaction of the ASME 1994. Volume 116.

A method of left heart ventricle contractility investigation

Juliusz L. Kulikowski, Malgorzata Przytulska, Diana Wierzbicka
Polish Academy of Sciences, Institute of Biocybernetics and Biomedical Engineering, Warsaw, Poland

Introduction: The methods of processing of biological objects representing images play a substantial role in biological investigations as well as in medical diagnosis. In particular, computer-aided methods of image analysis make it possible not only to evaluate static parameters, but also to conduct qualitative and/or quantitative examination of time-varying biological objects. This work concerns a computer-based method of serial images analysis elaborated, in particular, for ultrasound imaging used in left cardiac ventricle regional contractility investigation.

Ventricles' contractility is one of basic indicators of heart function. A Fourier spectrum of the function describing the variations of left chamber's shape contains useful diagnostic information about sector and

time contractility pathologies. An examination of regional ventricles' contractility leads to the detection of local cardiac dysfunctions like wall motion akinesis, diskinesis or hypokinesis. There is presented a mathematical model of left chamber shape variations within a single heart-beating cycle. The model is given in its direct and incremental forms. The methods of model coefficients evaluation based on the investigation of a series of cardiac images is described.

Basic Model Assumptions

The shape of a left chamber can be described by a positive real function

$$r(P,t) \equiv r(\alpha p, \varepsilon p, t) \qquad (1)$$

representing the distance between the centre 0 of polar co-ordinates located inside the inner contour of the chamber and a current point P on the contour. The polar co-ordinates $[\alpha p, \varepsilon p]$ of P describe the azimuth and elevation angles, correspondingly. The time t belongs to a real discrete time axis D.

In our kinetic model [2] it is assumed that $r(\alpha p, \varepsilon p,, t)$ is periodical with respect to all variables; the lengths of periods are 2π for αp, π for εp and T for t, where T is a mean length of a time-interval between two consecutive maximum diastolic chamber states. This model can be used for regional left chamber contractility, but not for long-term heart beating irregularity investigation.

As a periodic function $r(\alpha p, \varepsilon p, t)$ can be expanded into a 3-dimensional trigonometric series. The series is finite with respect to all indices, which is the result of limited model accuracy assumption as well as of a finite number of cardiac images capturing within the time-interval T. Therefore, the number of trigonometric series coefficients, i.e. the model coefficients being to be evaluated on the basis of a series of cardiac images, is also limited.

For the left chamber contractility investigation a modified, incremental version of the above-described kinetic model can be used. If we denote by δ, $0 < \delta < T/2$, a time-interval length between two consecutive image acquisition actions, then we can take into account a series of differences:

$$D_k(P) = r(P, k\delta] - r(P,0), \quad k = 1, 2, \ldots, K, \qquad (2)$$

where r(P,0) corresponds to the initial (diastolic) state and K is such that $T - \delta < K\delta < T$. The differences $D_k(P)$ are also periodic functions of αp and εp and can be represented by finite trigonometric series. The coefficients of $D_k(P)$ expansion into trigonometric series contain full information about the ventricle contraction process. We were particularly interested in investigation of their behaviour as functions of discrete time k.

Method: The method used in our investigations consisted of three basic steps:
1. Serial images pre-processing
2. Automatic shapes contouring
3. Time-series processing
4. Final contours refinement.

The results of automatic contouring of a series of images are shown in Fig. 3.

Fig. 1. A series of cardiac USG images with automatically restored left ventricle contours.

Typical envelopes of a time-series of shape coefficients are plotted in Fig.2.
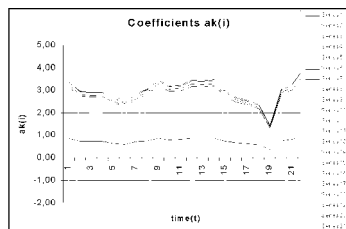
Fig. 2. Functions representing time-variations of typical cardiac left ventricle's shape coefficients.

In cardiac diagnosis a particular interest is paid to detection and evaluation of left ventricle contractility disorders, hidden in the form of $D_k(P)$ function.

Discussion: The kinetic model of left chamber shape variations in time describes well the regional chamber's contractility phenomena.

The model has been used in automatic contouring of the left ventricle in a series of cardiac USG images.

Using the time-series smoothing technique to the shape coefficients of the model a series of refined contours of the object under observation can be obtained, and so, the time-variations of its shape can be examined.

It is possible to evaluate the model coefficients effectively on the basic of computer-aided analysis of series of cardiac images obtained in USG modality, non-invasive for the patients.

References
[1] J.L. Kulikowski. "Mathematical Models for Computer-aided Analysis of Heart Ventricle. Part I: Static Models". Biocybernetics and Biomedical Engineering, vol. 17, Nos 3-4, 1997.
[2] J.L. Kulikowski, M. Przytulska, D. Wierzbicka. "Mathematical Models for Computer-aided Analysis of Heart Ventricle. Part II: Kinetic Models". Biocybernetics and Biomedical Engineering, vol. 19, No 4, 1999.
[3] J.L. Kulikowski, M. Przytulska, D. Wierzbicka. "Automatic contouring and a method of analysis of serial USG images in examination of left cardiac ventricle contractility disorders" (in Polish). Report of the Dept. of Biomedical Information Processing Methods, Inst. of Biocybernetics and Biomedical Engineering PAS. Warsaw, December 2000.

An implantable monophasic/biphasic atrial defibrillation system using transcutaneous RF power delivery

J A Santos[a], G Manoharan[a], N E Evans[a], J McC Anderson[a], B J Kidawi[b], J D Allen[b] and A A J Adgey[b]
[a]N Ireland Bioengineering Centre, University of Ulster, Northern Ireland, UK
[b]Royal Victoria Hospital, Belfast, Northern Ireland, UK

Aims & Background: Fibrillation is a chaotic electric excitation of the myocardium and results in a loss of the coordinated mechanical contraction characteristics of normal heartbeats. Atrial fibrillation (AF) is the most common arrhythmia, characterised by irregular and chaotic fibrillatory waves that replace the normal P wave of the QRS complex in the ECG. Current methods for defibrillation have varying success rates, risks and cost implications. The aim of this project is to realise a versatile passive implant to effectively treat AF in a risk-cost effective manner.

Methods: In this work we have accomplished defibrillation using a novel transcutaneous technique to deliver a unipolar DC pulse to a passive, battery-free implant. The system consists of a radio frequency (RF) on-off pulsed power source operating at 7.2 MHz and connected to an RF transformer; the latter is built with a series-tuned primary placed on the body surface and a parallel-tuned, intracorporeal secondary acting as the 'receiver.' The receiver's output is matched to the (nominal) 50 Ω resistive load presented by the heart and uses a Schottky diode half-wave rectifier to generate the unipolar stimulus. This is delivered to the load using two leads placed at the distal coronary sinus and atrial appendage.
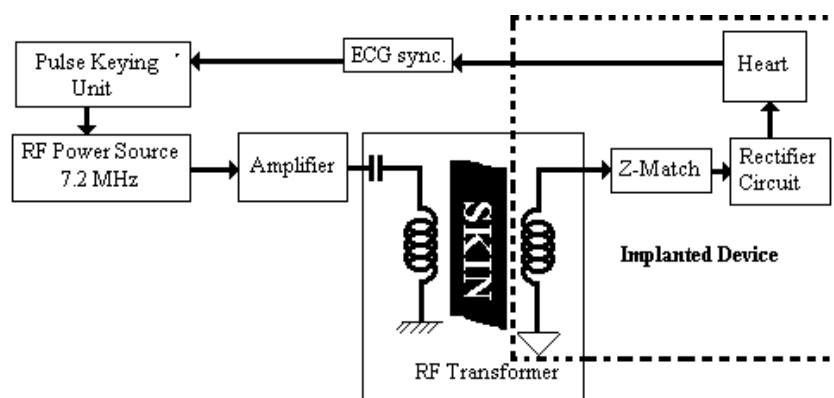
The device was tested using 10 anaesthetized sheep. Sustained AF was induced by rapid atrial pacing (Grass stimulator, 100 Hz, 5 V) and cardioversion was attempted, synchronized to the QRS complex. The efficacy of three pulse amplitudes (50, 75 and 100 V) was assessed using pulse widths in the range 5 - 30 ms. Defibrillation was repeated 5 times at each voltage and pulse-width setting. The delivered shock voltage and current were captured and stored for later analysis.

Based on the results obtained for this device, a modification was developed to obtain a biphasic waveform in the receiver unit; this accomplishes cardioversion with less pain and less damage to the heart tissue.

Results: In the monophasic device, at 50 V the rate of successful cardioversion was only 40 % for the smaller pulse widths, increasing to 74 % at 30 ms. Success rates were comparable at 75 V. At 100 V, however, 100 % success was observed for 10 ms pulses: this figure fell to 98 % when using 12 and 15 ms widths. The system proved resistant to lateral and angular coil misalignment, while maintaining high power transfer efficiency.

The biphasic device performance was simulated using analog circuit simulators to obtain the values for current and energy delivered to a 50 Ohm load. The total current at full power was 1.92 A, making the energy delivered 1.9 J. This biphasic device is currently being tested at the RVH, Belfast.

Volts	Width (ms)	5	6	8	10	12	15	20	30
50 V	% Success	18	40	48	50	56	64	74	74
75 V	% Success	-	-	52	58	66	66	78	-
100 V	% Success	58	72	88	100	98	98	96	98

Table 1: Cardioversion success rate for different pulse widths and amplitudes

Conclusions: During the experiments on the monophasic device, no arrhythmic complications were observed. Optimum coupling of the transmitting and receiving coils was achieved at 20 mm axial spacing. Complete success at 100 V and 10 ms, or 2 J delivered energy, indicates the strong potential of the technique. The absence of a battery makes the device attractive in terms of minimising potential hazard. This method is an inexpensive and viable alternative treatment for patients suffering paroxysmal AF.

References:
[1] BRONZINO, J.D. "The Biomedical Engineering Handbook," CRC Press & IEEE Press, 1995, pp.1275-1291
[2] HILLIS, L.D., ORMAND, J.E. and WILLERSON, J.T. "Manual of Clinical Problems in Cardiology," 1st Ed, Little Brown and Company, Boston, 1980, pp.13-14
[3] TIMMIS, A. and NATHAN, A. "Essentials of Cardiology," 2nd E., Blackwell Scientific Publications, 1993, pp. 228-239
[4] DONALDSON, P.E.K. "Frequency-hopping in r.f. energy-transfer links," Electronics & Wireless World, pp. 24-26, August 1986
[5] DONALDSON, N. and PERKINS T.A. "Analysis of resonant coupled coils in the design of radio frequency transcutaneous links, " Med. & Biol. Eng. & Comput., Vol. 21, September 1983, pp. 612-627

A new approach to the Holter events classification based on application of wavelet neural network

A. Wrzesniowski[a], E.J. Tkacz[b], P. Kostka[b]
[a]*ASPEL Medical Electronics Ltd., Kraków, Poland*
[b]*Institute of Electronics, Division of Biomedical Electronics, Silesian University of Technology, Gliwice, Poland*

Introduction: Contemporary cardiovascular system diagnostic process requires more and more sophisticated technical facilities and method to ensure the proper diagnosis quality and reliability. Therefore many biomedical engineering centers, both scientific and commercial make search towards new methods allowing implementation in the new diagnostic products. In case of Holter method ECG examination usually the problem of template extraction and further events classification should be solved out. Existing systems apply so called traditional methods requiring definition of several templates from 2-4 leads and then construction of classification process based on comparison of incoming morphology of QRS complexes from particular channel to the established set of templates by calculation of certain factor (e.g. MSE). However, such a classification process, accepted in most cases, has many disadvantages and thus follows the decrease of classification precision and reliability.

Methods: The main idea of new classification process construction is based upon the application of Wavelet Neural Network (WNN), where the first layer of artificial neural network consists of feature extractor built with a help of application of Wavelet Transform (WT). This idea comes from the observation of current tendency to combain different methods or signal processing tools together and creating in such a way new possibilities, which use positive features belonging to each of particular method. In our case the wavelet layer works as an initial template feature extractor which forms the vector of numbers describing characteristics of template morphology.

After wavelet transform [Fig.1] the created vector of features describing QRS complexes mophology is transferred to the artificial neural network structure for training. We have used for training the very common back propagation algorithm. The trained neural network is able then to classify the incoming QRS complexes to the groups of extracted previously templates.
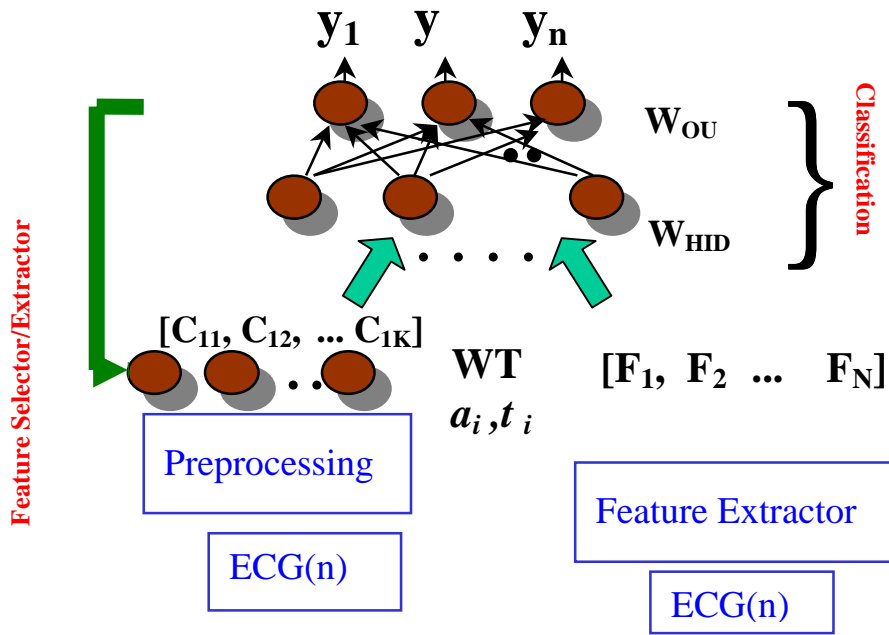
Fig.1: Block diagram of WNN structure

Results: Implementation of presented algorithm proved that combining two methods from generally understand signal processing area set of tools, leads relatively easy to creation or construction of a new approach concerning classification of Holter events. The sensitivity and specificity of the presented method concerning QRS complexes classification obtained through the simulation in Matlab environment was 93% and 89% respectively.
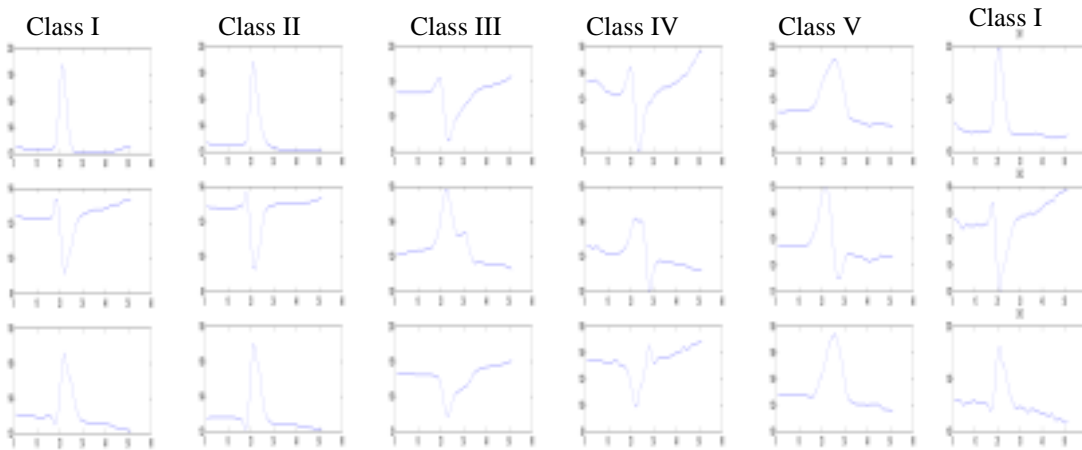
Fig.2: Set of extracted templates and result of classification

Discussion: Fig.2 presents an example results of classification obtained through the simulation. Five classes of 3-leads QRS complexes have been extracted from the real Holter system examination file and then transferred to the neural network for training. After that the incoming set of complexes (most right draw in fig.2) has been classified to class I. The next step relates to application of the state of the art technology (e.g DSP), which will hopefully lead us to creation of a new classification device

References

[1]   E.J. Tkacz, P. Kostka. An Application of Wavelet Neural Network for Classification Patients with Coronary Artery Disease Based on HRV Analysis. World Congress on Medical Physics and Biomedical Engineering - Chicago 2000

[2]   P. Kostka, E.J. Tkacz, Z. Nawrat, Z. Ma ota. An Application of Wavelet Neural Networks (WNN) for Heart Valve Prostheses Characteristics. World Congress on Medical Physics and Biomedical Engineering - Chicago 2000

Session – Biomedical Instrumentation, VR and Robotics in Medicine (or Instrumentation and VR)
Room 3, Friday 4 May, 16.15 – 17.30

Study of magentic three-dimensional localizer for endoscope

H. Zheng[a,b], D. Lin[a,] X. Chen[a], J. G. Hughes[b], N. D Black[b]
[a] Institute of Biomedical Engineering, University of Fuzhou, China
[b] Faculty of Informatics, University of Ulster, Northern Ireland, UK

Introduction: Doctors have used endoscopes (usually after an initial X-Ray scans) in conjunction with localisation techniques to discover and locate tumors, cancerous growths and other abnormalities. Endoscopes are inserted into the body and directed through various vessels until an abnormality is found. Once an abnormality has been found it is necessary to determine its exact location.

Location is determined using one of several localisation techniques. The most common of these is the use of X-Rays. X-Rays provide a two dimensional view of the body and the position of the endoscope within it. However a 3D view is required to discover the exact location of the endoscope and the abnormality it has found. Numerous X-Rays can be taken from various angles to provide this 3D view. This is not ideal, though, as patients cannot be exposed to X-Rays for prolonged periods.

Research suggests two further alternatives: ultrasound and magnetic localisers. Ultrasound localisers provide a 3D position of the endoscope by calculating distances or directions between the endoscope and the ultrasound transmitter. Placed on the surface of the body, the ultrasound transmitter sends synchronised pulses that are picked up by a receiver placed on the tip of the endoscope. Ultrasound offers the advantage that it can be used for non-rigid objects such as the endoscope. Further to this it means X-Ray exposure is restricted to the mandatory dosage required to determine that an abnormality exists. A disadvantage of ultrasound, though, is that it has difficulty locating the endoscope as the signals may be obstructed or minimized by some bodily organs such as the lung.[1]

An alternative approach is in the use of magnetic localisers. This is our area of study. This aim of this project is to develop a localiser that determines a 3D position of an endoscope by using an external magnetic field, determines the posture (direction and rotation) of the endoscope using a 3D magnetic sensor at the tip of the endoscope and finally to navigate a trace of the endoscope inside the body to reduce the X-Ray dosage. This paper introduces results of work done in the laboratory thus far.

Methods: Three mutual orthogonal magnetic fields are set up outside the body and three mutual orthogonal magnetic sensors are attached to the tip of the endoscope. The localiser contains a controlling circuit, power amplifier, magnetic transmitting loops, magnetic receiving sensors and a PC processing system.

The controlling circuit generates a carrier wave and time control signals. These are used to generate timed bursts of electric current to create 3D magnetic fields. Before inserting the endoscope an external reference position for the tip of the endoscope is determined. As the endoscope is inserted and moved through the body the sensors on the tip of the endoscope induce changing magnetic fields. The field changes are converted to electrical signals containing position and posture data, which are returned to the PC processing system. The 3D position and posture of the probe is calculated by inserting the returned data into formulas in MATLAB. We use an elliptical integration function to determine the X, Y and Z positions of the endoscope in 3D.

Assuming that the tip of the endoscope is at an arbitrary position P, the magnetic transmitting loops are the X-, Y- and Z- loops; the magnetic receiving sensors are the *x*-, *y*- and *z*- loops and the angles from each of the three axes are *a*, *b* and *c*. The magnetic field strength, B Tesla, is calculated by:

$$\begin{bmatrix} B_X(x,y,z,a,b,c) \\ B_Y(x,y,z,a,b,c) \\ B_z(x,y,z,a,b,c) \end{bmatrix} = \begin{bmatrix} B_X(x,y,z,a_0,b_0,c_0) \\ B_Y(x,y,z,a_0,b_0,c_0) \\ B_z(x,y,z,a_0,b_0,c_0) \end{bmatrix} T_X(a_0-a)T_Y(b_0-b)T_Z(c_0-c) \qquad (1)$$

Where T*x*, T*y*, T*z* are the angle transformation matrices:

$$T_X(a_0-a) = \begin{bmatrix} 1 & 0 & 0 \\ 0 & \cos(a_0-a) & \sin(a_0-a) \\ 0 & -\sin(a_0-a) & \cos(a_0-a) \end{bmatrix} \qquad (2)$$

$$T_Y(b_0-b) = \begin{bmatrix} \cos(b_0-b) & 0 & -\sin(b_0-b) \\ 0 & 1 & 0 \\ \sin(b_0-b) & 0 & \cos(b_0-b) \end{bmatrix} \qquad (3)$$

$$T_Z(c_0-c) = \begin{bmatrix} \cos(c_0-c) & \sin(c_0-c) & 0 \\ -\sin(c_0-c) & \cos(c_0-c) & 0 \\ 0 & 0 & 1 \end{bmatrix} \qquad (4)$$

In order to reduce any interference to the magnetic fields, the carrier wave is transmitted in different phases. First it is sent at 0^0 and then at 180^0. The average of the returned data from the sensors is adopted.
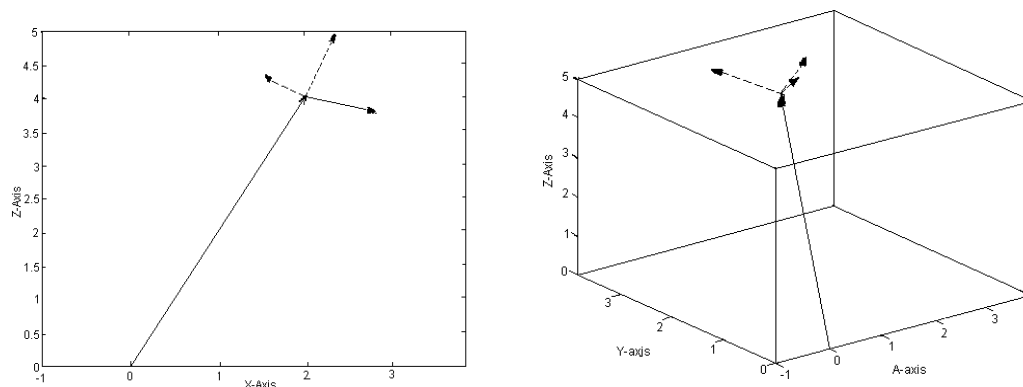
Two methods to display the tip of endoscope at Position (2,3,4) and Status (10,20,30), view (0, 0, 0)

Result and Discussion: The position and posture of the tip of the endoscope can be displayed in MATLAB in several ways. The tip is shown as position (2,3,4) with angles of (10,20,30). A 3-D model (r.h.s) gives a good representation of position and posture. However to gain more detailed information we use a 2-D view (l.h.s) of the X-, Y- or Z- axes.

Laboratory research is still being conducted. A key goal in the research is to reduce the size of the receiving sensors, as current sensors are too large for insertion in the tip of an endoscope. Further experiments will be carried out using these smaller sensors to determine both their effectiveness and accuracy.

Reference
[1]   Shinich Tamura, Xin Chen, Jiang Kai, etc. 3D localizer for ultrasound endoscope by an outside-body marker, SPIE proceedings Vol. 3241

PathFinder: a new image guided robot for neurosurgery

Patrick A Finlay
Armstrong Healthcare Limited, High Wycombe HP13 7AG, UK

Background: The ability to place instruments accurately on a target deep inside the brain is a basic requirement in neurosurgery. In practice, an accuracy of 1mm is sufficient for the most demanding clinical tasks.

Interest has grown in recent years in a method of registering images to patients using a robotic arm. The accuracy is acceptable, with an average total error of around 2 - 3 mm, and a minimum error (in the well conditioned region of the envelope) of around 1mm.

PathFinder is a surgical robot designed to maximise the benefits of image guided surgery. Using PathFinder the surgeon can specify a target and a trajectory on a medical image. This information is then converted into robot movements which cause an instrument guided by the robot to be positioned in precisely the desired location. Registration and tool calibration are carried out semi-automatically, and obstruction of the surgical site is minimised.

Description: The PathFinder system consists of a planning workstation and a positioning robot. Use of PathFinder involves two stages: pre-operative planning and surgical implementation. Medical imaging of the patient precedes these, which is outside the scope of PathFinder.

The PathFinder planne will accept any DiCom3 compatible modality of image, but will normally expect to receive CT or MRI scans. Before imaging, the patient must be fitted with fiducial skin markers in the form of 3mm diameter titanium spheres bonded to a black disk.

The PathFinder workstation displays three orthogonal views of the patient. The surgeon uses the mouse to specify a target point inside the brain and an entry point on the cranium.

The PathFinder robot is a 6-degree of freedom revolute manipulator of roughly human arm dimensions, mounted on a wheeled trolley The robot permanently holds a camera in its end effector, and uses this to register the medical image to the real patient. The robot moves in a pre-programmed arc over the approximate position of the patient's head and detects the fiducial marker positions. It then moves closer and measures the position of each marker by taking two views to allow stereo range finding. A template-matching algorithm is then used to fit the image co-ordinates to the patient.

The same camera measures the length and offset of the surgical instrument to be used. The surgeon can then instruct the robot to move the tool to a point immediately above the chosen entry point. When the robot has reached this point, brakes are automatically applied to each axis and electrical power is removed from the motors.

PathFinder's basic powered tooling has a single linear axis. Some instruments, including biopsy probes, additionally require a second rotary axis, and many instruments require special energy sources at the tip, for example electrodes, cryo-probes and suction devices. A safety interlock prevents the main robot axes from being moved while the instrument axes are active, and vice-versa.

The requirement for delicate manipulation is solved by using tool holders which can detect subtle changes in forces and torques corresponding to tissue boundaries, and respond accordingly. These devices are under development.

Safety Issues: A key safety device is the footswitch, which the surgeon must depress to permit robot or instrument motion. Releasing the footswitch at any time stops the robot. The robot speed is limited to a slow motion in each axis, and the robot arm is fitted with contact detectors which will stop motion in the event of a collision or entrapment. The instrument drive includes force sensing which will stop movement in the event of excessive forward force being detected, or if a lateral movement is made, for example by inadvertent movement of the patient clamp. The camera held in the robot end-effector can be used to check registration if movement is suspected.

A hazard analysis has been carried out on the robot with the aim of eliminating sources of single-point failure. As a result of this analysis, further safety features have been incorporated. These include the duplication of robot axis encoders, and the development of a supervisor which monitors robot position as measured by both sets of encoders and stops movement in the event of a mis-match. The kinematic analysis used in the secondary encoders has been separately calculated and encoded from the first. The supervisor and joint-level control of the robot is encoded in Ada on an embedded processor which has a purpose-written BIOS to avoid any errors which may be present on commercial operating systems.

Conclusion: PathFinder represents an innovative approach to frameless stereotaxy, in which the automation of registration and calibration has produced a robotic localiser of high accuracy and considerable user-friendliness.

Instrumentation and algorithms for monitoring cognitive task performance

P.J McCullagh[a], R. Howard[a], Lim Ai Lian[b] and C. Misir[b]
[a]Faculty of Informatics, University of Ulster, Northern Ireland, UK
[b]Department of Psychology, Nationa, University of Singapore, Singapore

Introduction: Event related potentials, ERPs [1], have been used by the psychophysiologist to study attention, memory and learning and as a tool to investigate mental dysfunction. With the use of appropriate paradigms, ERPs may also be used in the non-invasive investigation of human brain function to provide insight into cognitive processing and to study emotion. Where a recording system is in place, and some programming expertise is available, it is possible to implement an ERP system using a standard multimedia PC for presentation, as this set-up possesses the attributes required for cognitive studies:
- flexibility in the configuration of stimuli;
- synchronisation of the presentation events to the recording of the EEG;
- ability to set response requirements and to monitor the subjects' compliance

Methods: The presentation instrumentation comprises a standard multimedia PC for visual presentation (VIS) linked to the PC based EEG recording system. The latter system was implemented using physiological amplifiers controlled by a PC based data acquisition system (ACQ) and bespoke software [2]. Connecting the serial interfaces of both PCs and amending the data acquisition software facilitated synchronisation of the software processes. As the acquisition software was time critical, it acted as a master, initiating a presentation sequence. The presentation software was written in Borland Delphi 4, and provided modules for:
- Visual stimulus presentation from standard image files
- Setting subject response requirements
- Reaction time computation and performance monitoring
- Auditory and visual feedback to the subject
- Asynchronous communications interface, using Tcomport [3]

The system is completely configured by software and many categories of ERP can be elicited, including cortical, P300 and contingent negative variation components. The following experiment investigated changes in category and location of stimulus (left visual field, L and right visual field, R) and may be categorised as a 3-stim experiment [4].
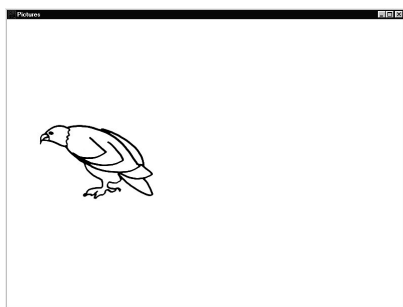
Figure 1 Sample stimuli for a sweep illustrating a category change

Table 1 Location and category changes and response requirements

Condition	Change	Cue Stimulus, S1	Target Stimulus, S2	Response
1	none	L,C1; L,C2; R,C1; R,C2	L,C1; L,C2; R,C1; R,C2	None
2	Location	L,C1; L,C2; R,C1; R,C2	**R**,C1; **R**,C2; **L**,C1; **L**,C2	Left 'z' key
3	Category	L,C1; L,C2; R,C1; R,C2	**R**,C1; **R**,C2; **L**,C1; **L**,C2	Right '/' key

Table 1 illustrates the various presentation options and Figure 1 illustrates a sample condiition. Each acquisition sweep comprises two stimuli presented to either the left or to the right fields of the graphics screen. The subject is instructed to respond differentially to category changes and location changes.

Results: Figure 2 provides an event sequence diagram, which illustrates inter-process communication for a single trial. It comprises the following steps:
- ACQ determines the category of image and image number, and sends this information to VIS at the start of the trial.
- After a prestimulus ACQ instructs VIS to show the current image (S1)
- S1 is displayed for 1 second, and then erased
- A second image (S2) is then displayed for up to 2 seconds. The subject must according to the instructions of the paradigm
- VIS determines the reaction time RT of this keypress and extinguishes (S2). Depending on how quickly the subject complied, a reward in the form of points is given.
- VIS provides auditory feedback using the multimedia player.
- ACQ's recording window and inter-trial interval, are set to ensure that VIS has completely finished this sequence of events before the start of the next recording sweep.
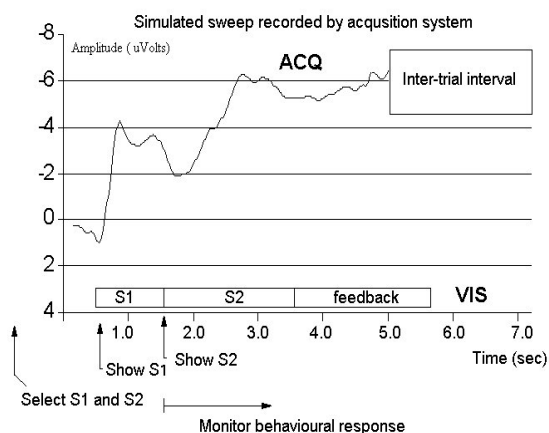
Figure 2 - Event sequence diagram for a single sweep.

Discussion: The three areas of image presentation, subject monitoring and communications with an external recorder are central to this area of ERP recording and form the basis of other ERP programs. The performance of the graphics update is a crucial issue in a real-time system, as any time delay will be mirrored in the electrophysiological recording. In this experiment the images comprise small line drawings, which take up little memory space. Whilst the author has resisted the temptation to incorporate graphics accelerators, the case for the inclusion of the TComPort is unanswerable.

References

[1] T.W. Picton and S.A. Hillyard, Endogenous event-related potentials. In: Picton TW, ed. Handbook of Electroencephalography and Clinical Neurophysiology Vol 3: Human Event-Related Potentials, [Amsterdam:Elservier, pp. 361-426, 1988.

[2] P.J. McCullagh, H.G. McAllister, M.F. Regan. Multichannel data acquisition and analysis of EEG and event related potentials, Innovation et Technologie en Biologie et Medecine, 13, No 6, pp. 693-703 (1992).

[3] Crnila D. TComport. Delphi source code available via internet http\\delphi.stts.edu.

[4] J Katayama and J Polich. P300 from one-,two-, and three-stimulus auditory paradigms. Int J Psychophysiol 1996; (1-2):33-40.

Application of CNC milling and reverse engineering for the manufacture of titanium cranioplasty implants

W. Mc Knight[a], J. Winder[b], B. Lewis[c]
[a]*Manufacturing lecturer, University of Ulster, Northern Ireland*
[b]*Principal Clinical Scientist, NI Medical Physics Agency, Northern Ireland*
[c]*Prosthesis Laboratory, School of Dentistry, RVH, Belfast, Northern Ireland*

Introduction: A review into the manufacture of titanium cranioplasty inserts concluded that 23% were described as poor fitting and 41% of frontal plates had poor aesthetic quality (1). The use of rapid prototyping, stereolithography (STL), in titanium cranioplasty was introduced at our institution to improve the fit and aesthetic quality of the titanium implants (2). Patient's with a skull defect needing repair had a routine Computed Tomography (CT) scan. Normally, the skull defect was built up manually on a stereolithography model using wax to produce a smooth and continuous contoured skull surface. The model was then used to manufacture a forming die from dental stone. The forming die in conjunction with a high-pressure fluid cell press would accurately form 0.25mm titanium plate to replicate the skull geometry. Finally the plate was trimmed to fit over the defect.

This method had three main limitations. Firstly, STL models are dimensionally unstable as they are hydroscopic. Secondly, they are expensive and therefore the skull models previously built were limited in size and usually only a small portion of the skull was built. This limited the amount of information of the patient's skull that was used in making a new contour to provide a good cosmetic outcome. Model build time was typically twelve hours and costs ranged from £400 to £1000. Thirdly, the subsequent manufacturing processes to produce the actual titanium plate was a highly skilled and labour intensive process. We propose an alternative manufacturing strategy that utilises the benefits of reverse engineering and associated Computer Aided Design (CAD) and Manufacture (CAM).

Proposed Alternative Method of Model Manufacture: Computer Numerical Controlled (CNC) milling was chosen for modelling as it can manufacture in a wide variety of materials, has high accuracy and could be programmed using the same original STL data file. The STL file was prepared as before and imported into a CAM (Delcam PowerMill V3.01) system to generate the digital code for the CNC milling process.. The model was produced in a dimensionally stable and rigid modelling board (Cibatool BM5460). Build time was reduced significantly and cost was of the order £250.00.

Application of Reverse Engineering And Time Compression Methodologies: The CNC manufacturing process provided a cost effective solution for the reproduction of a skull model. However, the major advantages are to be achieved by eliminating a considerable portion of the manual skill required in the subsequent processes to produce the titanium plate. Integrating reverse engineering and CAD

(Delcam PowerShape and AutoCAD 2000) technology into the process is proposed as a method to introduce substantial time compression and cost saving advantages. Figure(1) shows a rendered CAD

model of a skull with a left hand size defect. CAD software was then used to fit a 3D surface controlled by the overall skull shape. Figure(2) shows a 3D CAD generated surface fitted over the skull defect.

This computer based procedure would replace a number of manual steps used to produce the titanium plate and would significantly reduce the lead time and manufacturing cost required to convert a skull model into a titanium cranioplasty. Additionally, the CAD surface data now provides the required geometrical information to manufacture the actual titanium implant via the fluid cell press. The surface implant geometry can be graphically inverted, a suitable forming die modelled and manufactured by the CNC milling process.

Figure 1
Rendered CAD image showing
left hand side cranial defect

Figure 2
Rendered CAD image with
superimposed 3D surface

Conclusions: We have developed an alternative method for the manufacture of custom titanium cranioplasties using CNC milling. The advantages over the previous technique include faster lead time to manufacture the model with significant cost reduction. Also the application of CAD software has enabled reverse engineering of the skull defect and will further streamline the labour intensive process of making custom titanium cranioplasties. Surgeons can be provided with a cost effective CNC manufactured model of the skull and can interactively participate in the design, fixing, verification of a virtual computer generated surface patch and verification of the manufactured titanium implant upstream of the actual operation.

References
[1] Joffe J.M., McDermott P.J.C. and Linney A.D. Computer genrated titanium cranioplasty:report of a new technique for repairing skull defects. British Journal of Neurosurgery (1992), 6, 343-350.
[2] Winder J., Cooke, R.S., Gray J., Fannin T. and Fegan T. Medical Rapid Prototyping and 3D CT in the manufacture of custom made cranial titanium plates. Journal of Medical Engineering and Technology (1999), 23(1), 26-28.

The idea of virtual lungs application to ventilatory support testing

T. Golczewski, M. Kozarski, M. Darowski, M. Guc
Institute of Biocybernetics and Biomedical Engineering, Polish Academy of Sciences, Warsaw, Poland

E-mail:tgol@ibib.waw.pl

Introduction: New methods of ventilatory support require testing before their application to medical practice. Tests on living models need both models and laboratories, hence they became more and more expensive, and ethic problems inherited in such tests are crucial. The use of physical models of the lungs is not perfect, too. Either such models are evidently too simple to reflect complex lungs properties or they are too expensive and difficult to build and modify. Both kinds of models are poorly observable.

The above problems forced us to consider a different approach (Fig.1)**:** to test physical respirators with the use of virtual lungs (**VL**). Indeed: (1) VL need not laboratories, etc. (thus low costs), (2) there are not any ethic problems, (3) VL may be as complex as our knowledge and skill allow to be, (4) VL are easily modifiable and completely observable.

Fig.1. The main idea: a real respirator ventilates the virtual lungs instead of a living model or a physical one.

Virtual lungs: Since not a human being but the respirator is a "user" of VL, VL need not reflect, for example, 3-D lungs structure. "The respirator world" consists of the air flow and the pressure, and thus VL has to reflect accurately only the dynamic relationship between the flow and the pressure. Hence it appears that such a VL has to be rather a functional than anatomical model of the lungs. However, to be a virtual object, such a model has to be sufficiently complex to be able to behave accurately under conditions not determined precisely before the model building.

Fig.2 shows schematically our initial model, which is used as VL. Its most characteristic features: a separation of the lung and the chest (the subscript "w" for the chest), and a partition of the lungs into five lobes having non-linear viscoelastic properties (the subscripts "1" to "5"). Parameters for the "ordinary lung" have been collected on the basis of widely accessible literature (cited in [1]). Their modifications reflect different diseases and malfunctions. Fig.3 shows an example of adequacy of our VL.

R/V - V/R converter: Since the respirator and VL have to affect one another, they have to be joined by means of real-to-virtual and virtual-to-real (R/V, V/R) converters (Fig.1). If the human uses virtual reality, then usually: the monitor is the V/R converter, and the mouse or joystick is the R/V one. Here, however, the respirator is the main "user" of VL. Therefore, our converter ([2], patent pending), which has a gyrator structure, transforms pneumatic variables into electrical ones read by a computer (R/V), and reversely (V/R). Certainly, the human can observe effects of respirator influence on VL in the monitor.

References
[1]   M.Darowski, M.Kozarski, T.Golczewski. Model studies on respiratory parameters for different lung structures. Biocybernetics and Biomedical Engineering 20: 67-77 (2000)
[2]   M. Kozarski, M.Darowski, J.Glapinski, E.Krauze. A new approach to simulate repiratory system mechanical properties. Lecture notes of the ICB seminars, Warsaw, Sept.1997 : 73-78.
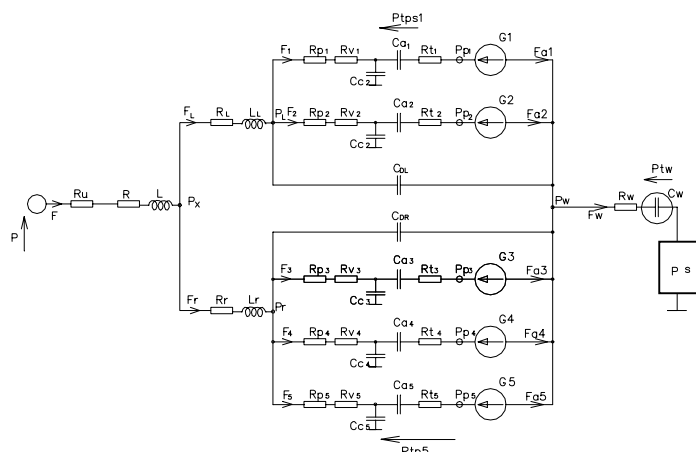
Fig.2 The model that is used as the virtual lungs (shown approximately with electrical symbols). The P variable (the F variable) on the left is the output of the R/V (the input of the V/R) converter.

Changes of the lobes volumes as a percentage of their end-expiration volumes (for two exemplary depths of the inspiration). a) the right upper lobe, b) the middle, c) the right lower one.

Fig.3 Differences in the ventilation of the particular lung lobes for the vertical position of the patients due to the gravitational effect.

Session – Biomedical Processing and Modelling
Room 3, Saturday 5 May, 09.00 – 10.30

Application of bioimpedance to in vivo. Breast cancer detection

N. Chauveau[a], P. Martel[b], S. Freitas[b], B. Rigaud[a] and J.P. Morucci[a]
[a] *INSERM U455 CHU Purpan 31059 Toulouse Cedex France*
[b]*Institut Claudius Regaud, 20 rue Pont St Pierre, 31000 Toulouse, France*

Introduction: The early detection of breast cancer remains an important problem of public health. There is a great emphasis in trying to develop non invasive in vivo techniques which could be repeated more often and with good confidence.

Bio-electrical impedance can detect electrical properties change in cancerous tissues in ex vivo as reported by Fricke et al [1], Surowiec et al [2], and Jossinet and Schmitt [3]. Even if the results are not as good as microscopic examination, they prove the existence of an observable difference between normal and pathological tissues. Heinitz and Minet [4] proposed a two electrode impedance needle to measure the tumour in situ, permitting the classification of 5 kinds of tumors. More recently Moskovitz [5]

published a work using the T-Scan, a new non invasive industrial device based on electrical impedance measurement. Our approach is also based on a non invasive in vivo bioimpedance technique.

Methods: We use a XITRON 4200 impedance analyser. The device measures the bio-electrical impedance using a 4 electrode technique, in a frequency range from 5 kHz to 1 MHz. We have developed a specific program to drive the device from a PC via a serial link. This program permits to achieve a full sweep of frequency analysis in about three seconds. Data are displayed on a Bode diagram for validation before backup. Each measure is carried out using 4 disposable hydrogel Ag/AgCl electrodes (SKINTACT$^{®}$) equally spaced.
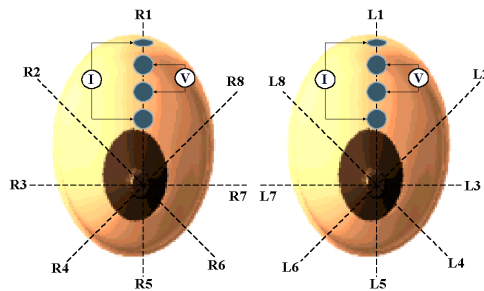
Fig. 1 The 8 electrode positions

The electrode positions are numbered from 1 to 8 using opposite rotation order between right and left to preserve the symmetry (figure 1). By this way R1 and L1 are comparable up to R8 and L8. A group of 20 patients presenting a diagnosed cancer type T2 (size more than 2 cm in diameter) has been investigated. A previous study [6] on normal subjects has proved that electrical bioimpedance greatly varies between subjects and breasts. Therefore we have calculated the impedance difference between right (R) and left (L) breasts for each subject. Most of the patients were presenting an infiltrating ductal carcinoma. We applied on each breast the four electrode system successively at the 8 locations. For each position, we analysed the relative module difference between right and left breasts defined by Δ%

$$\Delta\% = \frac{\text{Mod}(R) - \text{Mod}(L)}{[\text{Mod}(R) + \text{Mod}(L)]/2} \times 100$$

Fig. 2: Example of measurement with a cancer in left breast at position 7.

The technique can be improved by using a different electrode hand piece system. The surface of the electrodes and the size of the hand piece could be slightly reduced to measure a smaller area. More the volume measured is concerned by the tumour alone, more sensitive is the measurement. But on the other hand, smaller is the probe system and weaker is the sensitivity of the method because of reduced deep current lines.
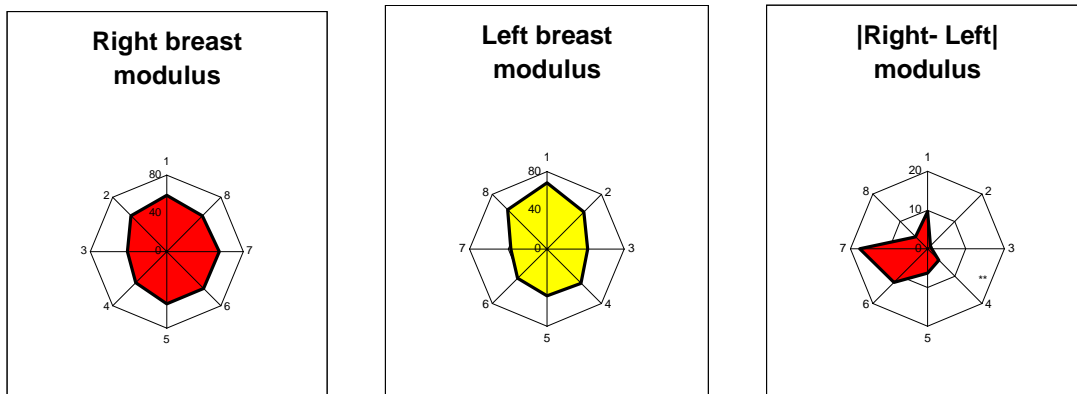
The principle of cancerous tissue detection in breast by using electrical impedance is challenging. Electrical bioimpedance is likely to take an important place in breast cancer detection in the next coming years.

References
[1]   H. Fricke and S. Morse, J. Canc. Res., 10, 1926, pp 340-376.
[2]   A.J. Surowiec, S.S. Stuchly, J.R. Barr and A. Swarup, IEEE Trans. On Biom. Engin., 35, 4, 1988, pp 257-262.
[3]   J. Jossinet and M. Schmitt, Annals of the New York Academy of Sciences, Vol. 873, 1999, pp 30-41.
[4]   J. Heinitz, O. Minet, IX Int. Conf. Electrical Bio-Impedance, Heidelberg, Sept. 26-30, 1995, pp 336-359.
[5]   O. Moskovitz, Proc. RSNA'96, 1996.
[6]   N. Chauveau, C. Thalamas, B. Rigaud, O. Rascol, JP Morucci, Proc. 5th Conf. Eur.Soc.for Engineering and Medicine, Barcelona, 1999, pp 515-516.

Determination of EEG activity propagation during voluntary finger movement

J. Ginter Jr., M. Kaminski, K. J. Blinowska
Laboratory of Medical Physics, Warsaw University, Warsaw, Poland

Introduction: A study of the voluntary motor tasks opens the possibility of brain-computer interface design [1]. It was found that the planning and the execution of voluntary movement is connected with pre-movement desynchronization (ERD) and post-movement synchronization (ERS) in the brain areas involved in the given task. Up to now, mainly amplitude properties of EEG during voluntary movements were considered [2]. We propose application of a method, called SDTF, which takes into account a phase information and makes it possible to determine EEG activity propagation as a function of time and frequency. The method is based on multichannel (not pair-wise) treatment of the signals. The vector of signals is simultaneously fitted to the model.

Material and Method: The experiment has been performed on three volunteers. EEG was registered from 24 electrodes positioned over motor, sensory, and (partly) visual cortex areas and referenced to linked ears. The signal was sampled at frequency 256 Hz. Movements of index finger, registered by a microswitch, were performed 5 seconds after silent sound generated every 10 to 14 seconds. The EEG signal was divided into 8 second long periods, with movement onset in the 5th second.

SDTF, similarly to introduced earlier Directed Transfer Function (DTF) [3], is defined in the framework of multichannel autoregressive model (MVAR). Non-normalized DTF (describing flow of the signal from channel j to channel i) is expressed as the non-diagonal element H_{ij} of the transfer matrix of MVAR. In a case when multiple repetitions of the task are available the coefficients of the MVAR model and hence transfer matrix can be calculated for short-time epochs by averaging over trials. In this work MVAR model was fitted to the 80-sample long window, then the window was shifted by 10 samples. The bootstrap method was used to evaluate the errors. Since the coupling between hemispheres estimated by means of coherence, was found to be low, the model was fitted simultaneously to 12 channels situated in the same hemisphere (left or right).

Results: The SDTFs, representing the intensity of EEG flows were found as the functions of time and frequency. For the electrodes situated above sensorimotor areas connected with the finger movements broadband breaks in the EEG activity flows were observed from 1 second before to 1 second after the start of the movement. At that time EEG propagation from the electrodes located close to sensorimotor areas, connected with leg and face, was observed. One second after movement, an increase of EEG propagation in the beta band was found for electrodes Fc1, Fc3, C3 and Cpz (Fig. 1 and 2).

Discussion: The propagation from the locations outside the sensorimotor areas supports the hypothesis of focal-ERD/surround-ERS hypothesis [2]. Additionally to the increased activity in the leg area reported earlier [2], we have also observed increased EEG outflow from the facial area. The strong propagation in the beta band from the frontal derivations Fc1, Fc3 is in agreement with MEG measurements [4]. The time course of the beta activity flows suggests the ways of communication between different parts of somatosensory and motor cortex, and gives an evidence of cross-talk between different brain structures.

SDTF method proved to be a useful tool in establishing the patterns of flows in a short time scale, due to truly multichannel treatment of the time series. Pair-wise estimation of causality between channels can be misleading, especially when channels of a process are connected by complicated mutual relationships as is the case for EEG. In comparison to DTF, which proved to be powerful method for the time scale of the order of seconds SDTF makes possible estimations of EEG flow changes in the order of tenths of miliseconds. We believe that the SDTF method should carry over to many other useful applications.

References

[1] Pfurtscheller G., Flotzinger D., Kalcher J. Brain-Computer Interface — a new communication device for handicapped persons. Journal of Microcomputer Applications 1993; **16**:293-299.

[2] Pfurtscheller G., Lopes da Silva F. H., Event-Related Desynchronization, Handbook of Electroencephalography and Clinical Neurophysiology, Revised Series, Vol. 6, 1999 Elsevier Science B. V.

[3] Kaminski M., Blinowska K. J. A new method of the description of the information flow in the brain structures. Biological Cybernetics 1991; **65**:203-210.

[4] Samelin R., Hari R. Spatiotemporal characteristics of sensorimoror neuromagnetic rhythms related to thumb movement. Neuroscience, 1994; **60**:537-550.

Fig. 1. Time course of SDTF in the beta band (15-30 Hz). The corridor of errors at the level of one standard deviation is shown

Fig. 2. Flows of EEG activity during resynchronization in the 15-30 Hz band represented by ratios of SDTF in epoch 1-2 s after movement to SDTF in epoch 5-3 s before movement. The flow of the activity directed toward electrodes at the tips of arrows.

In vivo measurement of the skull conducitivity: EIT versus SEP/SEF

S.Gonçalves [a,b], J.C. de Munck [a] and J.P.A. Verbunt [a]
[a] *MEG Centre VUMC/University Hospital Vrije Universiteit, The Netherlands*
[b] *Institute of Biophysics and Biomedical Engineering, University of Lisbon, Portugal*

Introduction: The Inverse Problem (IP) of EEG [1] aims to estimate the sources inside the brain based on measurements of the electrical potential on the scalp surface being assumed that the head is divided into a number of compartments, and that the *equivalent* conductivities of these compartments are known. Large systematic errors in the localisation of the sources may arise due to errors in the values of the conductivities, which are taken from literature and vary over a wide range [2].

In this study we use the principles of Electrical Impedance Tomography (EIT) and the combined analysis of somatossensory evoked potentials (SEP) and somatossensory evoked fields (SEF) to determine these equivalent conductivities in vivo.

Methods: The feasibility of the use of EIT to determine the equivalent conductivities of brain, skull and scalp that decrease the systematic errors of the EEG IP has been proved theoretically in [2]. Here, we prove the practical feasibility of the method by comparing its results with the results obtained with an independent method: SEP/SEF analysis.

EIT and SEP/SEF data were recorded from 5 different subjects using the CTF Inc. MEG/EEG system. Spherical and realistic models were used to describe the head (brain, skull and scalp). The solution to the EIT forward problem in the spherical case can be found in [2]. The combined analysis of the SEP/SEF data applied in the spherical model case is performed in two steps. First a dipole is fit to the MEG data and afterwards EEG data is used to fit the conductivity of the brain, the brain to skull conductivity ratio and the radial component of the dipole.

The realistic head model was built from MRI scans of each subject and the forward problem of EIT was solved using the Boundary Element Method [3].

For both methods, the cost function used in the IP was defined in a [generalised] least squares sense.

Results: According to the conclusions in [2] it appears that if the head model is affected by some geometrical error, then EIT estimated conductivities would also be affected by an error compensating the geometrical error. Therefore, when using the spherical model with the same relative skull thickness for all subjects, some variation in the skull to brain resistivity ratio might be expected. The results presented on table 1 confirm this (note:subject 4 did not show any useful somatossensory response on the EEG). A comparison between spherical and realistic models, for EIT, is presented on table 2.

Discussion: This study demonstrates the practical feasibility of the proposed EIT method to estimate equivalent electrical conductivities of brain (σbrain), skull (σskull) and scalp (σscalp). The results of ρskull/ρbrain obtained with the spherical model show a significant variation among subjects. This is confirmed by the SEP/SEF analysis, which is a completely independent method both in principle and in technical characteristics. This spread considerably decreases with the use of realistic models. We think that the observed variability arises from the geometrical errors committed by taking spherical models with the same relative skull thickness for all subjects, this error being considerably decreased by taking the realistic model with the correct skull thickness for each subject. However, even in this situation some variability is still observed, which can be attributed to natural causes.

This study shows the importance of using this EIT method routinely as a part of EEG modelling.

	EIT	SEP/SEF
Subject	$\rho_{skull}/\rho_{brain}$	$\rho_{skull}/\rho_{brain}$
1	31	43
2	93	85
3	68	55
5	66	74

Table 1. Results of in vivo measurements of the relative resistivity of the skull obtained by two different methods.

Subject	Spherical	model	
	ρ_{brain} (Ω.cm)	ρ_{skull} (Ω.cm)	$\rho_{skull}/\rho_{brain}$
1	435	13278	31
2	278	25858	93
3	295	20059	68
4	255	31602	124
5	245	16072	66
	Realistic	model	
1	321	14925	46
2	281	14502	52
3	316	14670	46
4	262	17083	65
5	358	6127	17

Table 2. Results of in vivo measurements of the resistivity of brain and skull obtained with EIT.

References
[1] Z.J Koles *Electroenceph. Clin. Neurophysiol*, 106, 127-37 (1998)
[2] S. Gonçalves,J.C. de Munck, R. M. Heethaar, F. H. Lopes da Silva and B.W. van Dijk, Physiol. Meas., 21, 379-393 (2000)
[3] T. Oostendorp, A. Oosterom, IEEE Trans Biom Eng, 38, nº5 May, 409-417 (1991)

Automatic detection of sleep stages using the EEG

P. Van Hese,[a,b] W. Philips,[c] J. De Koninck,[d] R. Van de Walle[a] and I. Lemahieu[a]
[a]Elis Department, MEDISIP, IBITECH, Ghent University, Belgium
[b]Department of Neurology, Ghent University Hospital, Belgium
[c]Telin Department, Ghent University, Belgium
[d]Department of Neurology, St.-Vincentius Hospital, Deinze, Belgium

Introduction: An electroencephalogram (EEG) is a measurement of the time-varying potential differences between electrodes fixed on the skin of the head (scalp). The EEG is an important clinical aid used by the neurologist for the diagnosis of sleep disorders. Sleep is categorized into two different types: Non-REM sleep and REM sleep. During sleep, the brain follows cycles, each lasting approximately 90 minutes. The cycle begins with Non-REM sleep consisting of stages one to four. Then, the stages quickly reverse, reaching REM sleep. A review of the EEG can reveal unusual patterns. A complete manual inspection of a long-term sleep EEG recording or scoring is a time-consuming and difficult task. A method to facilitate the review is highly needed. To extract relevant information from the EEG, a number

of parameters can be defined in the time and frequency domain. We present a method that uses a number of these parameters to come to an (semi-) automatic detection of the sleep stages.

Method: The method we developed consists of four steps: segmentation; parameter extraction; cluster analysis; and classification. In the segmentation step, the EEG is broken down into sections with a fixed length, called segments. We choose the segment size to be 10 s because we had the manual scoring for the sleep EEG in steps of 10 s. Three sets of parameters were compared: the parameters of Hjorth [1] (activity, mobility and complexity), the harmonic parameters (bandwidth, center frequency and value at center frequency) and the relative band energy (energy in 7 frequency bands divided by the total energy). Each parameter is calculated for every segment resulting in a parameter vector associated with the respective segment. All parameter vectors lie in a *n*-dimensional vector space. In the third step, the cluster analysis, we form a number of clusters (a group of parameter vectors spatially close to each other) in the vector space by using the k-means algorithm. We choose *k* equal to 20, and afterwards reduced the number of clusters to 5 by grouping some clusters so that non-spherical clusters could be modelled. The final step is the classification. Every segment (parameter vector) is classified according to the classification of each cluster the segment belongs to. A total classification of the EEG thus only requires the manual classification of the centres of the clusters.

Results: To verify the method we applied the algorithm to one 6-hour sleep EEG recording, which had been manually scored by an experienced neurologist. We used one EEG channel to calculate the parameter vectors mentioned above. The vector space obtained by using the harmonic parameters is depicted in figure 1 for the channel F7-T7 and this for the first 2 hours of the EEG. The regions (clusters) corresponding to the different stages are indicated.
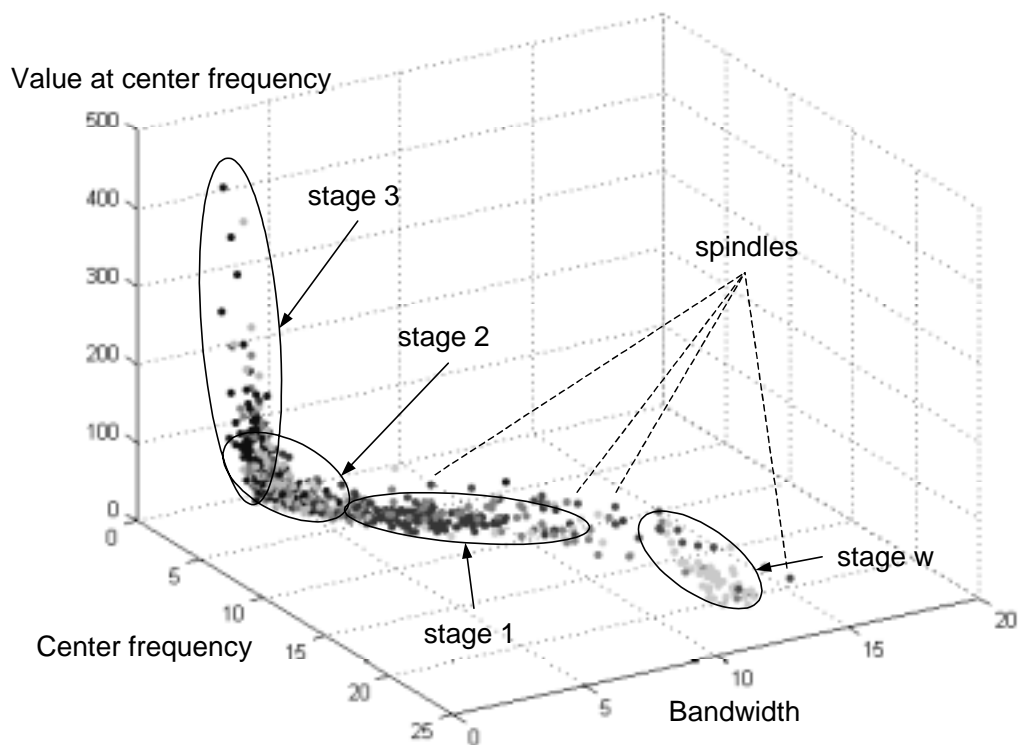

Figure 1. The vector space constructed with the harmonic parameters for the channel F7-T7.

Discussion: Figure 1 shows that stage w (awake) and stage 1 can be clearly distinguished. Stage 2 and 3 are overlapping. This overlap makes the automatic detection harder. However, it should be noted that even neurologists have difficulty in classifying the different stages without using extra information (e.g. ECG and EOG). The conclusions for the other sets of parameters (Hjorth and relative band energy) are very similar. Furthermore, automatic detection of the sleep stages is complicated by the presence of so-called sleep spindles, short waveforms (2 to 3 s) with a frequency of 12 to 14 Hz. The parameter vectors associated with these spindles are scattered in the constructed vector space. A clustering algorithm as k-means searching for spherical clusters has difficulty of classifying these spindles correctly. We suggest altering the method so that in a first step the spindles are being detected and in a second step the detection of the sleep stages follows, without taking into account the segments containing a detected spindle. Probably the method will perform better if the information contained in all the channels is being used. In addition, the method has to be validated using the EEG from different patients.

References
[1]   B. Hjorth. Time domain descriptors and their relation to a particular model for generation of EEG activity, 1974
[3]   Kaminski M., Blinowska K. J. A new method of the description of the information flow in the brain structures. Biological Cybernetics 1991; **65**:203-210.
[4]   Samelin R., Hari R. Spatiotemporal characteristics of sensorimoror neuromagnetic rhythms related to thumb movement. Neuroscience, 1994; **60**:537-550.

Mathematical model of autonomic nervous systems

A.Martynenko, M.Yabluchansky, B.Kantor
National University, Kharkov, Ukraine

Introduction: The autonomic nervous system (ANS) mathematical modeling is of great interest for development of non-invasive diagnostics, though recently it earns less attention compared to experimental research methods [1]. To fill the above gap a non-bulky model has been elaborated with a minimum number of inner parameters which reflect nevertheless main physiological mechanisms of the cardiovascular system rapid control loop. For the reason of ANS model improvement and additional physiological facts the earlier suggested model was revised. Non-linear operation which realized in natural life unlike technogenic sphere was used in the new model [2].

Materials and methods: Undoubtedly quasiperiodical processes underlying cardiovascular system functioning determine specific mathematical analysis technics of heart rate, blood pressure series, ventricular pressure or peripheral resistance etc. This technics statistically standardized by The European Society of Cardiology and The North American Society of Pacing and Electrophysiology. Spectral analyses of time series evaluate as «quasi» character of periodical process. Each heartbeat according to this analysis is estimated as significant event and cool periodic is corresponding to direct line on rythmogramm. Methronomized rhythm is characterized as last degree of cardiovascular dysregulation and is a strong predictor of sudden death. Rhythmogramm of healthy subject is described as signal of stochastic source. That is fundamental property of nonlinear dynamic processes and is distinctive sign of selforganized systems.

For us it is important and undoubted fact that cardiovascular system and control complex is periodical nonlinear dynamic system. This fact is the main point for further development of knowledge about ANS and transition from formal spectral analyses of heart rate variability (HRV) to real modeling of ANS

functions integrated with cardiovascular biomechanic. Such approach is widening methodological base of ANS function analyses and diagnostic possibilities of HRV evaluation methods.

Accordingly to idea about regulation of cardiovascular action and their reflection by HRV we postulate that the main ANS characteristics can be described as nonlinear dynamic periodical processes in humoral, sympathetic, parasympathetic branches of nervous system.

Additionally we should write down equations that describe function of biomechanical parameters forming ANS activity. The last equation describes HR changes from cycle to cycle. Heart rate continualization (HR) is seems to be natural due to continuity of cardiovascular regulatory process and continuity of biomechanical functions. The diagram determines connections between components of equations.

Each of differential equations describes periodical process which has own frequency characteristics. Obviously, ABP frequency is coincide with HR and available for direct measurement. Frequency of uninterrupted function HR will be tally with HR only on condition of lack of regulatory systems influence. In that case physician will see direct line on rhythmogramme, the sign of full autonomy of frequency function. What is more each of modeling functions will be strictly periodical only in case of destroy of described on diagram connections and autonomy of corresponding equation. Thus, ANS mathematical model (MM) created by such a way that on the one hand it describes autonomic dynamic processes in a case of gross cardiovascular pathology. On the other hand MM planed as component of model for registration of variability because established relations and their mutual influences describe all observed changes in ANS-CVS.
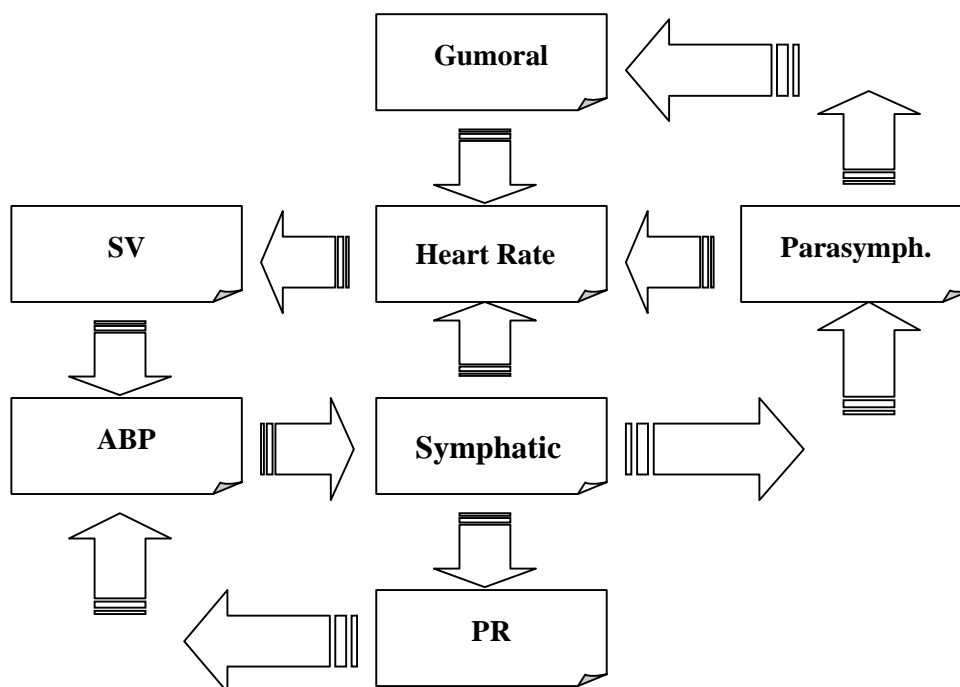
Results: Comparison of modeling results and measured data (ECG and rhythmogramm) and individualization for each patient parameters of model are possible by solution of reverse task and optimization of coincidence criteria of prognostic and registered data. Such a criteria is closeness of distributed (for example, rhythmogramm) and integral (for example, ratio of spectral zones power) characteristics of ANS. It is important to note that creation of model completeness at biomechanical level

provided completely by noninvasive methods. It is required only make out a standard form, which includes: age, sex, height, weight and ratio Systolic BP/Diastolic BP.

Conclusion: The mathematical model of autonomic nervous system (ANS) is introduced for correct and individual reproduction of all phenomenon registered by ECG. MM gives us the new possibilities for the more deep understanding of cardiovascular regulatory systems functioning, for improvement of ANS-cardiovascular dysfunction diagnostic. Also this model is useful tool at the level of regulatory systems assessment for monitoring of ANS-cardiovascular function and prediction of pathological processes development and results of therapeutic care. Only simple non-invasive procedures are required for computer modeling.

References
[1]   M. Yabluchansky, B.Kantor, A.Martynenko Heart rate variability in modern clinic.-Donetsk: Buden Publ., 1997.- 107 p.
[2]   M.Yabluchansky, A.Martynenko, A.Isaeva Practical handbook of heart rate technology for human regulation system investigation.-Kharkov: Osnova Publ., 2000.- 88 p.

Construction of a model of the torso for ecg problems based on cad tools and images of the human body

C. Navarro[a], J. Anderson[a], J. Allen[a], J. Toro[a], J. Riddell[b], A.A.J. Adgey[b]
[a]NIBEC, Northern Ireland BioEngineering Centre, University of Ulster, Northern Ireland
[b] Royal Victoria Hospital, Belfast, Northern Ireland, UK

Introduction: The governing differential (or integral) equation for the ECG problems with a corresponding set of boundary conditions must be solved in a domain that represents the human torso [1]. Simple domains that permit analytical solutions have been used in order to determine the effects of the closeness of sources to measurements, noise, inhomogeneities, etc. However, for a clinical use of the solutions of the ECG problems, it is necessary to use a realistic torso geometry that includes its physical properties. Boundary Elements or Finite Elements methods are frequently used to solve the governing equations. Because of the complex geometry of a torso, the mesh construction can turn out to be one of the most time consuming aspects of the modelling process.

As the modelling has progressed it has been possible to take information from CT or MRI regarding the anatomy of the thorax and create more complex and precise models of the thoracic volume conductor and its constituent parts [2]. Alternately, in this work the source for the geometrical information is obtained from images of a virtual cadaver [3]. In this web site, images of slices of a male and a female human bodies are presented. Manual segmentation of the slices that permits a description of some organs and bones and the use of a CAD application that facilitates the creation of 3D meshes provide a good balance between accuracy and speed in this modelling process.

Methods: Twenty slices equally spaced were taken from the 230th up to 730th slice. Contours of the heart, lungs, sternum, spine, fat layer and torso surface were obtained by means of manual segmentation. In order to obtain the surface of the intervening organs, the segmented slices were stacked to form a 3D description of the torso. In this way, using the CAD software I-DEAS [4] and some simple custom programs, a mesh was constructed. The triangled surfaces of the organs are shown in figure 1. For each organ and bone considered, a 3D mesh was separately generated using IDEAS. Also, surfaces that describe the fat layer and the torso surface were used to generate two additional 3D meshes. A custom

program processed the set of meshes in order to construct a unique mesh that reflects the different tissues under consideration. Additional smoothing to each organ in the general mesh was performed.
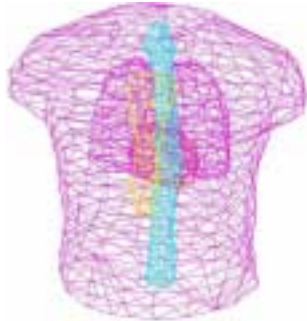

Fig.1. Triangled surfaces

Finally, 77 nodes on the torso surface were chosen to be the nearest to the corresponding electrodes location of the NIBEC harness [5]. Some of these nodes were slightly moved in order to increase its placement accuracy. In this way, the torso model can be used to do research with the forward and inverse ECG problems.

Results: In tables 1 and 2 some statistics of the mesh are presented.

Conclusion: An alternative procedure for constructing a realistic model of the torso that can be used in ECG problems have been outlined. The procedure permits the achievement of a good balance between accuracy and speed in constructing a 3D mesh. The geometrical information was taken from images of slices of a human body and the time-consuming work of programming routines for constructing a mesh was substituted by the use of an commercial mesher embedded in a CAD application.

Element type	Quantity of elements	%
Fat	3757	33
Heart	199	2
Lungs	751	7
Bones (sternum + spine)	361	3
General tissue	6336	55
TOTAL	11404	100

(1)

Node type	Quantity of nodes	%
Epicardium	59	2
Torso surface	1136	45
Other	1335	53
TOTAL	2530	100

(2)

Tables: Number of tetrahedral elements (1) and nodes (2).

References

[1]   Robert S. MacLeod, C. R. Johnson, P. R. Ershler, "Construction of an inhomogeneous model of the human torso Robert S. MacLeod, Dana H. Brooks, "Recent Progress in Inverse Problems in Electrocardiology", IEEE EMBS Magazine, pp. 73-83, January/February 1998.

[2]   for use in computational electrocardiography", IEEE EMBS 13th Conf, IEEE Pres., pp. 688-689, 1991.

[3]   http://www.npac.syr.edu/projects/vishuman/VisibleHuman.html.

[4]   http://www.sdrc.com.

[5]   Cullen C, Dempsey GJ, Wright GTH, McAdams ET, Anderson J, Adgey AAJ, "Body Surface Mapping in Mobile Coronary Care", Proc. 14th Conf. IEEE EMBS Pt. II, pp 796-797,1992.

Session – Cardiovascular, Imaging and Instrumentation
Room 3, Saturday 5 May, 16.15 – 17.30

New method of transoesophageal signal filtering during noninvasive electrophysiological study of the heart conductive system

K. Peczalski[a], D. Wojciechowski[a], Z. Niedbalski[b], M. Kowalewski[c], P. Sionek[a], G. Skoczylas[a], M. Stopczyk[a]
[a]*Laboratory of Clinical Bioengineering Institute of Biocybernetics & Biomedical Engineering PAS and Wolski Hospital, Warsaw, Poland*
[b]*Elmiko, Warsaw, Poland*

Introduction and method description: It is perhaps surprising that, despite the introduction of the electrocardiogram into clinical use early in this century, research on its role for the diagnosis of cardiac conductive system still continues. In the 1960s and 1970s, this continued interest was fuelled by the dramatic increase in knowledge of arrhythmia's that resulted from the introduction of invasive cardiac electrophysiology. In this method endocardial leads were connected to an appropriately isolated and filtrated ECG machine. The electrocardiograms, at various endocardial positions, could be displayed on a multichannel ECG recorder. During the examination different endocardial positions would be also paced using programmable external stimulator connected to an endocardial lead. This became the basis of a clinical electrophysiological study (EPI), which aim was to clarify the activation sequence of the heart and to determine refractory periods. However, the EPI method was traumatic because of introduction of leads to the heart via veins system. The long time required for the proper location of leads in various endocardial positions led also to a significant x-ray exposure of the patient and staff. Therefore a new diagnostic method, transoesophageal electrophysiological study, was introduced in 1970s. The special external stimulator was constructed in ITAM Zabrze Poland for such study. The method utilized the anatomical phenomenon of the short distance between the esophagus and the left atrium of the heart. Our paper describes improvements to this diagnostic method.

The results of EPI study used to be analyzed by a physician from very a long (several meters) ECG recording. The introduction of digital computer techniques allowed for automation of EPI system including equipment monitoring, recording and analyzing electrical data from the heart during electrophysiological studies. EPI catheters (leads) are inserted into the heart and connected to the amplifiers. The amplifier processes then digitizes the selected channels. This networking sends signal data to the computer system for the storage on optical or CD disc after the data is transmitted. At present time few such systems are offered by several commercial companies worldwide.

Technical problems referred to esophageal recording: The transoesophageal signal of the heart activity shows some differences comparing intracardiac signal. The most important differences are significantly higher than in intracardiac ECG pacing impulse artifact and the zero line fluctuation.

System description: The transoesophageal EPI system basic module provides complete digital ECG and transoesophageal ECG recording and reviewing in each of 16 channels. The system consists of analogue 12 channels biological amplifier (according to IEC – 601 standards), 12 bit analogue/digital converter, Pentium microcomputer with 4.2 GB HD, CD-ROM recorder, monitor, laser printer and ECG DigiTrack software.

Method for artifact discrimination: The artifact discrimination software system is proposed. The first order filter triggered by stimulating impulse is used. The parameters of filter were chosen experimentally.

Discussion: As mentioned above the transoesophageal signal of the heart activity versus intracardiac signal shows following differences: significantly higher than in intracardiac ECG impulse artifact and the zero line fluctuation. Artifact of pacing impulse depends on its duration and amplitude. For transesophageal capture biphasic impulse with 20 ms duration and about 10 V amplitude is needed. Amplitude of impulse varies from patient to patient. Such impulse created artifact covering of atrium response to pacing. Previously the hardware system zeroing of esophageal amplifiers input triggered by impulse was applied for artifact discrimination. We propose an improved software artifact discrimination system. For artifact filtering first order integrator at 8 Hz is applied. The onset of filtering is triggered by pacing impulse with 5 ms. delay. The duration the filtering process is optimized experimentally to be 20 ms. Several previous probes are averaged in order to avoid the abrupt changes in transesophageal record during filtering. The high pass filter with 3 Hz cut frequency is applied for filtering of zero line fluctuations. These methods of filtering provide the diagnostic usable signal from esophagus. Such signal can be utilized to activation sequences and refractory periods measurements.

References
[1] R. Sutton, *The Foundations of Cardiac Pacing*, Futura Publishing Company, New York, 1990.
[2] A. De Luna, *Clinical Electrophysiology*: A Textbook, 2nd Updated Edition, Futura Publishing Company, New York, 1998.
[3] D.Wojciechowski, K. Peczalski, P.Sionek, M.Stopczyk, *1998 Report*, Laboratory Of Clinical Bioengineering IBIB PAS, 1998.

Application of optoelectronic methods in monitoring of chemical sympathectomy

P.Lukasiewicz[a], W.Raciborski[b], A.Liebert[a], W.Staszkiewicz[b], R.Maniewski[a]
[a]*Institute of Biocybernetics and Biomedical Engineering PAS, Warsaw, Poland*
[b]*Department of Vascular Surgery, CPMS, Warsaw, Poland*

Abstract:. The optoelectronic methods for testing of the effectiveness of Chemical Lumbar Sympathectomy (ChLS) are presented. The examiantion is based on the intraoperative monitoring of the perfusion measured with the use of the laser-Doppler (LD) instrument and changes of the haemoglobin levels measured with the Near InfraRed Spectroscope (NIRS). The obtained results showed that the method presented allows for an early and non-invasive prediction of the long-time effect of the operation.

Introduction: The laser-Doppler flowmetry and near infrared spectroscopy are new non-invasive optical methods for the monitoring of the tissue perfusion and oxygenation [1,2]. However, because of the relative calibration, these methods are used mainly in clinical examinations, where stimulation is performed, e.g. occlusion, temperature or position changes. They seem to be also useful in some clinical interventions effecting the perfusion and oxygenation of the tissue. The aim of this study was to apply the laser-Doppler method and the near infrared spectroscopy for the evaluation of the efficiency of the Chemical Lumbar Sympathectomy. The ChLS is applied in the treatment of advanced lower limb ischaemia caused by the permanent spasm of the capillary vessels in the microcirculatory system. During the operation the dose of ethanol is administrated into the anterolateral area of the body at L_2 vertebral spine level. The alcohol denatures the group of the nerve fibres causing the spasm of the microcirculatory system of the lower limb. The effect of the ChLS is the opening of the capillary system vessels and significant increase of the microperfusion.
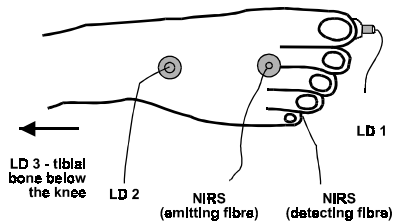

Fig.1. Placement of the LD and NIRS optodes during the sympathectomy

Method: The 15 ChLS operations were performed in patients with peripheral vascular diseases: the Burger's disease, chronic peripheral occlusive disease and diabetic ischaemic foot. The multichannel LD monitor Oxford Array (Oxford Optronix Ltd.) was used for the microperfusion and temperature measurements in three points of the lower limbs (Fig.1). The microperfusion was measured as the product of the concentration and the speed of red blood cells in the superficial layer of the skin. The tissue oxygenation was measured with the spectrometer NIRO-500 (Hamamatsu Photonics) applied on the foot in the transmitting mode. The changes in the tissue concentration of oxyhaemoglobin (HbO_2), deoxyhaemoglobin (Hb), total haemoglobin (Hb_{total}) were recorded. The recordings of the LD and NIRS signals were started 5 minutes before and finished 30 minutes after the ChLS procedure.

Results: Fig.2. presents the recordings of the perfusion and haemoglobin concentration for one of the patients studied during ChLS and immediately after this procedure. The results of the LD and NIRS measurements were classified as positive (see Fig.2.), if the following effects were observed: an increase of perfusion, an increase of oxyhaemoglobin (HbO_2), an increase of total haemoglobin (Hb_{total}) and an increase of the skin temperature. The clinical effects of the ChLS were evaluated three months after the operation. A good correlation between the clinical long-term effects of the ChLS and the results of the LD and NIRS monitoring was observed in 11 patients. No correlation between the clinical long-time effects of the ChLS and the results of the LD and NIRS monitoring was observed in 4 cases.

Conclusions: The correlation between the clinical effects of the Chemical Lumbar Sympathectomy and the changes in perfusion and tissue oxygenation measured by LD and NIRS methods was obtained in 73% of the patients studied. The proposed method of monitoring may allow for a preliminary evaluation of the ChLS effects during and immediately after the ChLS operation.

References

[1] Laser Doppler - 1994 Med.-Orion Publishing Company London, Los Angeles, Nicosia, eds. G.Belcaro, U.Hoffmann, A.Bollinger, A.Nicolaides

[2] C.E.Elwell, A Practical User Guide To Near Infrared Spectroscopy, Hamamatsu Photonics KK 1995.

[3] W.Raciborski, W.Hendiger, W.Staszkiewicz, P.Lukasiewicz, A.Liebert, R.Maniewski – "Chemical lumbar sympathectomy effects evaluated by laser-Doppler flowmwtry and near infrared spectroscopy – preliminary studies", 21st Conference on Microcirculation, Stockholm, June 4-7, 2000
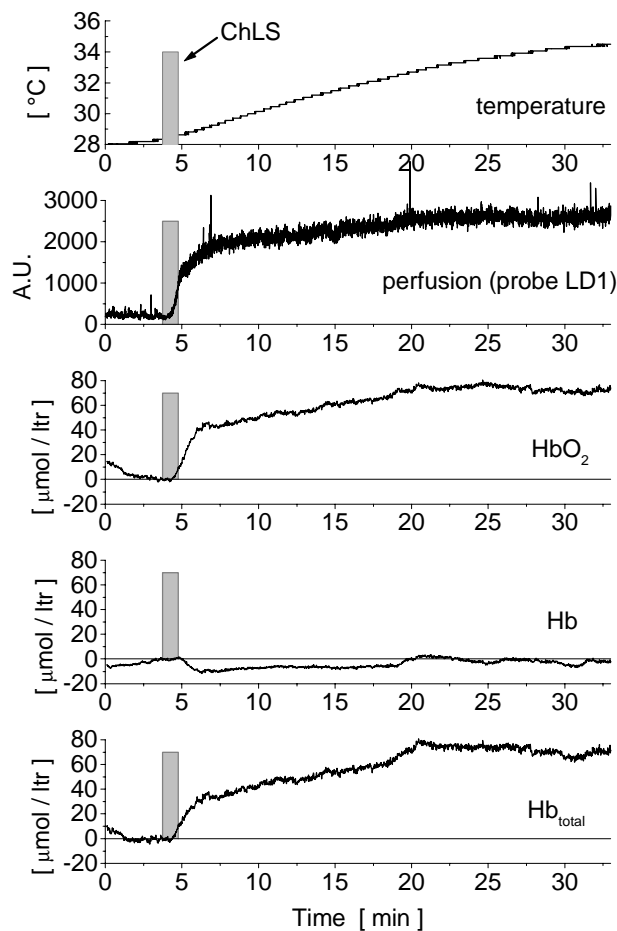
Fig.2. Example of the LD and NIRS recordings
during the ChLS

Near infrared spectroscopy for monitoring of cerebral oxygenation during carotid surgery

R.Maniewski[a], D.Gawlikowska[a], W.Staszkiewicz[b], A.Liebert[a], A.Gabrusiewicz[b], A.Zbie   [a]
[a]*Institute of Biocybernetics and Biomedical Engineering PAS, Warsaw, Poland*
[b]*Department of Vascular Surgery CPMS, Warsaw, Poland*

Introduction: Near infrared spectroscopy (NIRS) is a new non-invasive optical method for the tissue oxygenation and perfusion monitoring. The method is based on the specific chromophores absorption of near infrared light for various wavelengths [1]. In case of the cerebral tissue these chromophores, are: oxygenated haemoglobin, deoxygenated haemoglobin and oxidised cytochrome. The level of the changes of these chromophores depend on the cerebral oxygen supply. Besides, the total haemoglobin as the sum of oxy- and deoxyhaemoglobin corresponds to the cerebral blood flow, assuming that hematocrite remains unchanged. The purpose of this study was clinical application of NIRS in the monitoring of the cerebral tissue oxygenation and brain ischaemia, during carotid surgery. A particular attention was paid to the relation between the neurological state of the patients and the chromophores level, during the carotid artery cross-clamping.

Methods: The NIRS measurements were carried out with the NIRO500 (Hamamatsu Photonics, Japan) [2]. This system operates with four wavelengths of 775, 825, 850 and 904 nm. The optodes for the light transmission were fixed on the forehead and the frontal scalp, avoiding a close contact with the blood vessel and muscles. The interoptode distance was 4 cm. The following parameters were monitored and registered on the computer disc during the whole of the surgery procedure: oxyhaemoglobin (HbO_2), deoxyhaemoglobin (Hb) and oxidised cytochrome ($Cyt\ O_2$) concentration. The transcranial Doppler instrument equipped with a 2MHz pulse probe (EME TC or SONOMED TDS4) was used as the reference technique.

Results: Fig.1 presents the long-term recordings of HbO_2, Hb and Hb_{total} during the carotid endarterectomy in a patient with carotid stenosis. During the carotid test clamping period, a distinct decrease of HbO_2 and a reciprocal increase of Hb were observed followed by a stabilisation on almost a constant level after about 1 minute. This indicated sufficient collateral circulation, and, after short declamping, the carotid surgery was performed on this patient without intraluminal shunt insertion. Finally, the carotid declamping, after the surgery, influenced the rapid increase of HbO_2 and decrease of Hb, resulting in a substantial increase of the total haemoglobin level. Similar effects were observed in about 70% of the patients examined [3]. In the remaining patients, the carotid cross-clamping had no distinct effect or resulted in an immediate, rapid decrease of HbO_2 and increase of Hb signals with no stabilisation during the test clamping. The last group of patients showed insufficient collateral circulation and needed a shunt to prevent cerebral ischaemia.

Conclusion: The results of this study suggest that the near infrared spectroscopy is a sensitive method for cerebral oxygenation monitoring during the carotid artery cross-clamping. In spite of some individual variances between the patient, this method may be helpful in intraoperative cerebral monitoring, especially to indicate the necessity of the shunt insertion.

References

[1]   Litscher G. and Schwarz G. (Eds):Transcranial cerebral oximetry, Pabst Sci. Pub., Lengerich, 1997.
[2]   Elwell C.E.: A practical users guide to near infrared spectroscopy, UCL Reprographics, London, 1995.
[3]   Gawlikowska D., Staszkiewicz W., Gabrusiewicz A., Zbie   A., Maniewski R., Liebert A.: Experience with NIRS in surgical treatment of brain ischemia, Lecture Notes of the ICB Seminar on Optoelectronics in Medical Diagnosis, Warsaw, 1999, pp.78-82.
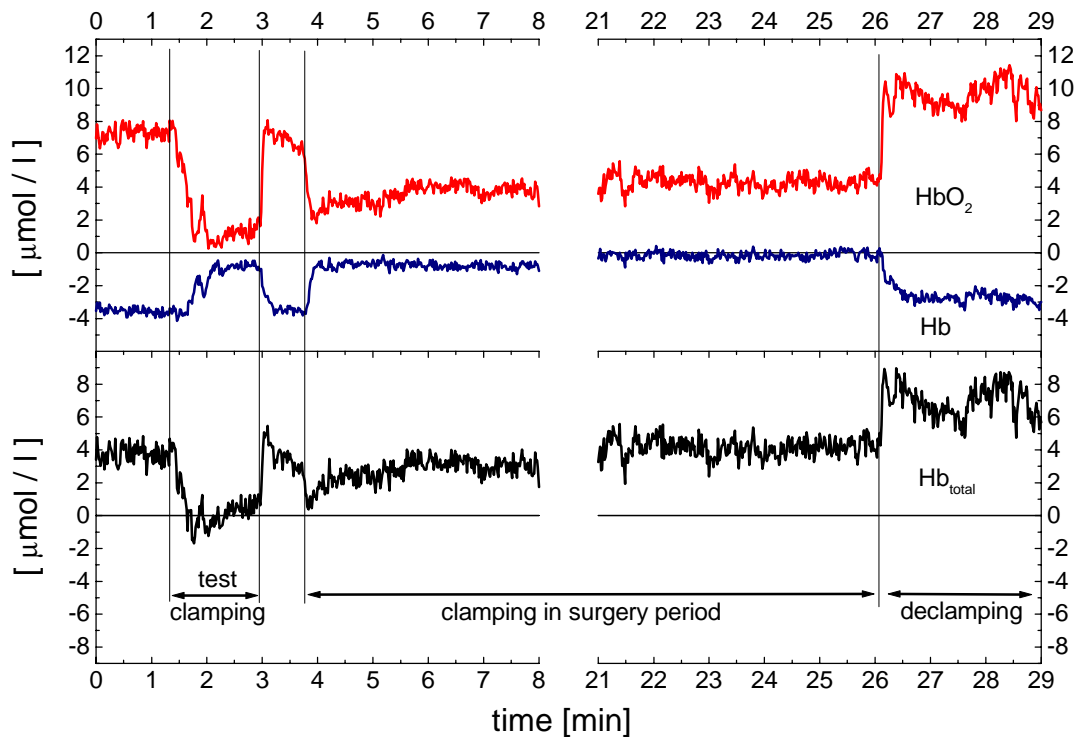
Fig.1. Oxyhaemoglobin (HbO₂), deoxyhaemoblobin (Hb) and total haemoblobin (Hb$_{total}$) recordings during carotid endarterectomy

Scanning electrical conductivity interfaces by means of ultrasound in magnetic field

A. Montalibet, J. Jossinet, A. Matias
National Institute for Health and Medical Research, INSERM U556, Lyon, France

Introduction: The propagation of ultrasound in a conductive medium in the presence of a magnetic field gives rise to a Lorentz force exerted on charge carriers. Since opposites charges are submitted to forces of opposite directions, the resulting effect is the creation of a bulk current density that can be shown proportional to the electric conductivity of the medium [1,2,3]. In the present study; the total current created in an object was collected using large surface electrodes. Specific signal processing enabled the visualisation of conductivity interfaces along the ultrasound path.

Equipment & Methods: A focused transducer generated 6 µs duration pulses at 500 kHz with a peak pressure of 1.5 MPa at a repeat frequency of 790 Hz. The magnetic field (350 mT) was created by a purpose-built, U-shaped magnetic circuit comprising NdFeB permanent magnets [4]. The measuring chamber consisted of a rectangular flask of transparent PVC (12 cm long, 4 cm wide and 12 cm high) open on the top. Two opposites sides consisted of ultrasound permeable membranes. The used conducting

models were 2x3x5 cm^3 cuboid blocks of agar gel. The gel was prepared with 9 g/l NaCl saline plus 25 g/l of agar powder. It was verified that the final conductivity of the gel was close to that of the initial saline. The current was collected by means of a pair of 9 cm long and 3 cm wide brass plates, parallel to the ultrasound beam and placed in contact with the upper and lower sides of the gel blocks (Fig.1). The electrodes were connected to a purpose-built dual input current-to-voltage converter (25 mS input admittance, 78000 V/A). The signal was recorded using a 420A Tektronix digital oscil-loscope (8-bit, 10 Ms/s, averaging mode: n=10000).
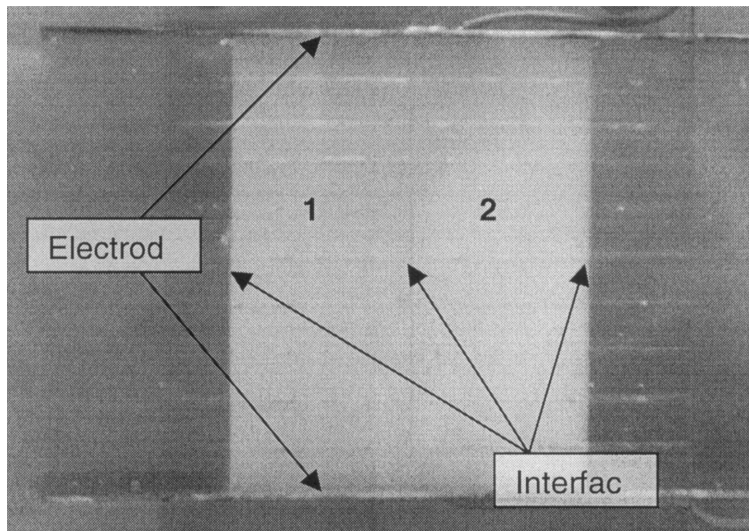

Fig. 1 : Agar model with 2 regions of equal lengths and different conductivity values ((σ_1=0.5 S/m, σ_2=1.4 S/m).

Results: The measured signal consisted of bursts at the same frequency as the ultrasound pulses. Inverse filtering was applied to the raw signal to retrieve the 1-D distribution of electrical conductivity gradients along the ultrasound path. Several filtering methods were considered [5]. In the present study, the signal was first windowed using a Blackman filter in the time domain. The spectrum of the windowed signal was then processed using a Wiener filter [5]. The final filtered signal was obtained by inverse fast Fourier transform. The signal shown in Fig. 2 is the response of a gel block comprising two regions of different conductivity values immersed in a non conducting medium. The signal duration shown in Fig. 2 is 600 µs ($\approx$ 9 cm). The interval between pulses was verified equal to the time-of-flight of the sound wave across each region. The 3 peaks observed correspond to the conductivity interfaces separating the 4 regions (0 S/m, 0.5 S/m, 1.4 S/m and 0 S/m).

Discussion: The complete theory shows that the final signal reconstructed according to the above method is proportional to the gradient of σ/ρ along the sound path. However, in the present study, the mass density ρ of the medium was practically constant. One may therefore consider that the signal of Fig. 2 reflected predominantly the changes in the electric conductivity of the medium.

Conclusion: The above results showed the feasibility of scanning electric conductivity interfaces with ultrasound. This method yields a new modality, termed Ultrasonic Lorentz Force Imaging (ULFI) [6] for bio-electrical tissue characterisation and imaging using ultrasound as a probe. Further studies include the

construction of multi-electrode systems and the development of algorithms for 2-D and 3-D image reconstruction.
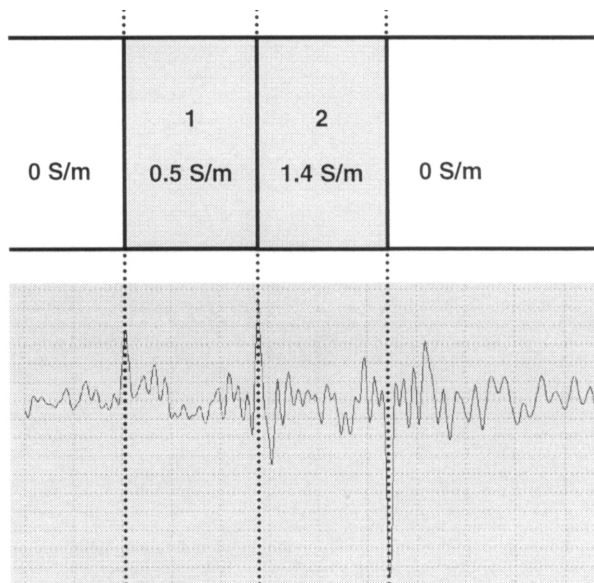

Fig. 2 : Final signal after Wiener filtering showing the conductivity interfaces between regions of different electric conductivities (0, 0.5, 1.4, 0 S/m, arbitrary vertical scale)

References
[1] B.J. Roth, P.J. Basser, J.P. Wikswo, "A theoretical model for magneto-acoustic imaging of bioelectric currents", IEEE Trans. BME-41: 723-728 (1994).
[2] H. Wen, J. Shah, R.S. Balaban, "An imaging method using the interaction between ultrasound and magnetic field", IEEE Ultras. Symp. : 1407-1410 (1997).
[3] J. Jossinet, B. Lavandier, D. Cathignol, "The phenomenology of acousto-electric interaction signals in aqueous solutions of electrolytes", Ultrasonics 36: 607-613 (1998).
[4] A. Montalibet, J. Jossinet, A. Matias, D. Cathignol, "Interaction ultrasound-magnetic field: experimental setup and detection of the interaction current", IEEE Ultras. Symp. : (2000, in press).
[5] M. Kunt, "Traitement numérique des signaux", Traité d'Electricité, d'Electronique et d'Electrotechnique (Dunod, 1987)
[6] A. Montalibet, J. Jossinet, A. Matias, D. Cathignol, "Electric current generated by ultrasonically induced Lorentz force in biological media" MBEC 27(1): (2001, in press).

Design of speckle denoising filter using wavelet-based thresholding for medical imaging application

Su Cheol Kang
Incom I&C, Seung Hong Hong, Dept. Of Electronic Engineering, Inha University, Doosan A.P.T 106-2303, Bongchun Bon-Dong, Kwanak-Gu, Seoul, 151-069, Korea(Rok)
Tel.: +82-2-885-1702; E-mail address rosette2@chollian.net

Summary: One of the most significant features of diagnostic echocardiographic images is to reduce speckle noise and make better image quality. In this paper we proposed a simple and effective filter design for image denoising and contrast enhancement based on multiscale wavelet denoising method.

Wavelet threshold algorithms replace wavelet coefficients with small magnitude by zero and keep or shrink the other coefficients. This is basically a local procedure, since wavelet coefficients characterize

the local regularity of a function. After we estimate distribution of noise within echocardiographic image, then apply to fitness Wavelet threshold algorithm.

Fully developed speckle of echocardiographic image has the characteristics of a random multiplicative noise. Theoretically, under the assumption that the real and imaginary parts of the speckle signal have zero-mean Gaussian density, speckle intensity can be shown to follow a Gamma distribution. Experimental speckle distributions can deviate from the theoretical Gamma distribution.

A common way of the estimating the speckle noise level in coherent imaging is to calculate the mean-to-standard-deviation ratio of the pixel intensity, often termed the Equivalent Number of Looks(ENL), over a uniform image area. Unfortunately, we found this measure not very robust mainly because of the difficulty to identify a uniform area in a real image. For this reason, we will only use here the S/MSE ratio and which corresponds to the standard SNR in case of additivie noise.

Standard speckle filters are the Median, Wiener, Gamma and Geometric filters. They usually perform efficiently on the most images. Wavelet-based filters are essentially based on a WCS approach that aims at obtaining an optimal trade-off between good signal averaging over homogeneous regions and minimal resolution degradation of image details. We have recently proposed such a filter, based on the Symmetric Daubechies(SD) wavelets.

We have concentrated on the best Signal-to-Mean-Square-Error(S/MSE) ratio provided by a complex Wavelet Coeffcient Shrinkage (WCS) filter and several standard speckle filter. Here we specifically address the numerical behavior of the WCS filter over a change in the regularity and type of the wavelet and in the wavelet coefficient thresholding type. We also measures of the variation of the S/MSE over a wide range of the WCS filter parameters in order to provide information on the optimal application range of the filter in practical situation.

We have simulated some echocardiographic images by specialized hardware for real-time application; processing of a 512*512 images takes about 1 min.

One example, the two images have very different spectral content in order to observe their effect on the filters performance. Two noise levels have been tested, coressponding to S/MSE ratios of 3.6 and 8.9 dB. The best S/MSE is provided by the complex wavelet filter with a soft-thresholding scheme.

Thus we have presented a numerical study of a complex WCS speckle filter that specifically addresses the change in regularity and type of the wavelet and in the wavelet coefficient thresholding type. We also gave measures of the variation of the S/MSE ratio over a wide range of filter parameters in order to get information on the optimal application range of the filter in practical situations. Test were performed on simulated imagery with a multiplicative Log-Normal noise. The S/MSE ratio was measured after averaging the filtered images over 16 diagonal shifts in order to approximate a shift-invariant DWT.

Our experiments show that the optimal threshold level depends on the spectral content of the image. High spectral content tends to over-estimate the noise standard deviation estimation performed at the finest level of the DWT. As a result, a lower threshold parameter is required to get the optimal S/MSE. The standard WCS theory predicts a threshold that depends on the number of signal samples only.